Journal Pre-proofs

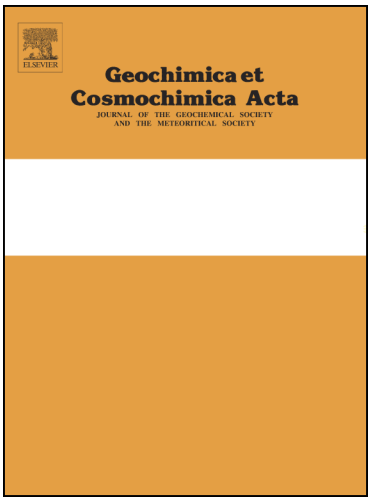

Clumped isotope effects of thermogenic methane formation: insights from pyrolysis of hydrocarbons

Guannan Dong, Hao Xie, Michael Formolo, Michael Lawson, Alex Sessions, John Eiler

PII: S0016-7037(21)00155-1
DOI: https://doi.org/10.1016/j.gca.2021.03.009
Reference: GCA 12123

To appear in: *Geochimica et Cosmochimica Acta*

Received Date: 3 July 2020
Revised Date: 20 February 2021
Accepted Date: 8 March 2021

Please cite this article as: Dong, G., Xie, H., Formolo, M., Lawson, M., Sessions, A., Eiler, J., Clumped isotope effects of thermogenic methane formation: insights from pyrolysis of hydrocarbons, *Geochimica et Cosmochimica Acta* (2021), doi: https://doi.org/10.1016/j.gca.2021.03.009

Clumped isotope effects of thermogenic methane formation: insights from pyrolysis of hydrocarbons

Guannan Dong[a*], Hao Xie[a], Michael Formolo[b], Michael Lawson[c], Alex Sessions[a], John Eiler[a]

[a] Division of Geological and Planetary Sciences, California Institute of Technology, Pasadena, CA 91125, USA
[b] ExxonMobil Upstream Integrated Solutions, Spring, TX 77389, USA
[c] ExxonMobil Upstream Business Development, Spring, TX 77389, USA

Revised after review for GCA, Feb. 20, 2021

ABSTRACT

Methane clumped isotope analysis is a tool used to constrain the formation or equilibration temperatures of methane, or to differentiate methane of thermogenic, microbial or 'abiotic' origins. Geothermometry applications are based on the temperature dependence of relative abundances of multiply-substituted isotopologues in thermodynamic equilibrium, whereas assignments of biogenicity or 'abiogenicity' rely on kinetic isotope effects associated with synthesis, which disturb clumped isotope abundances away from expected equilibrium proportions. However, kinetic processes in thermogenesis or during post-generation storage of thermogenic gas may cause isotopic disequilibrium, confounding thermometry applications or leading to 'false positive' identifications of microbial or abiogenic gases. Non-equilibrated clumped isotope compositions have been observed in thermogenic gases including unconventional oil-associated gases and from coal pyrolysis experiments. The isotopic disequilibria might be caused by kinetic isotope effects expressed during gas migration (including extraction), or by irreversible chemical processes, such as breaking carbon-carbon bonds in an alkyl precursor. In this study, we performed controlled pyrolysis experiments at 400°C on n-octadecane ($C_{18}H_{38}$). We characterized the gas chemistry, and compound-specific carbon and hydrogen isotope and methane clumped isotope compositions of the gas products. We found that $\Delta^{13}CH_3D$ values (anomalies relative to a stochastic distribution of isotopes) appear to be relatively close to equilibrium at the experimental temperature, whereas $\Delta^{12}CH_2D_2$ values are 30 to 40‰ lower than expected for equilibrium. The large deficit in $\Delta^{12}CH_2D_2$ can be explained by assembling hydrogen atoms affected by two distinct kinetic isotope effects into a methane molecule, previously referred to as a 'combinatorial effect'. We present a kinetic model that describes the full isotopic systematics, including anomalous $\Delta^{12}CH_2D_2$ deficits, of pyrolysis product methane. Finally, we propose a model for the isotope signatures of natural thermogenic methane where the non-equilibrium $\Delta^{12}CH_2D_2$ composition is a signature of the onset of catagenetic methane production. Our model also describes ways in which this signature disappears as further maturation drives $\Delta^{12}CH_2D_2$ to equilibrium through hydrogen exchange. Our findings demonstrate that anomalous depletion in $\Delta^{12}CH_2D_2$ is not a unique signature for microbial or putative abiotic methane, and specifically, it can be generated during pyrolytic chemistry.

[*] Corresponding author: gdong@caltech.edu

1. INTRODUCTION

The multiply substituted, or 'clumped' isotopologues of methane include two that are analyzable at high precision, $^{13}CH_3D$ and $^{12}CH_2D_2$ (typically at errors of 0.3 and 1.0‰, 1SE, respectively), using high-resolution mass spectrometry or infrared absorption spectroscopy (D.A. Stolper et al., 2014; Ono et al., 2014; Young et al., 2017; Gonzalez et al., 2019; Eldridge et al., 2019a). When methane is in internal isotopic equilibrium, the proportions of these doubly substituted species must conform to equilibria of isotope exchange reactions:

$^{12}CH_3D + {}^{13}CH_4 \rightleftharpoons {}^{12}CH_4 + {}^{13}CH_3D$ (R1)

$2\,{}^{12}CH_3D \rightleftharpoons {}^{12}CH_4 + {}^{12}CH_2D_2$ (R2)

The equilibrium constants for such reactions are functions of temperature; therefore, the relative abundances of non-, singly- and doubly-substituted isotopologues can constrain the temperature of methane formation or last equilibration. This approach to methane geothermometry is particularly useful because it permits a temperature estimate using only the isotopic composition of methane, without knowledge of isotope compositions of co-existing substrates, e.g., water, molecular hydrogen or kerogen. Such clumped isotope temperature estimates can constrain temperatures of natural gas formation or storage, contribute to reconstructions of the thermal histories of basins containing petroleum-forming systems, and differentiate thermogenic versus microbial methane (based on their distinct formation temperatures). However, all such applications of clumped isotope analysis to quantitative geothermometry require that methane forms and retains internal isotopic thermodynamic equilibrium. If instead methane forms out of thermodynamic equilibrium or is driven from an equilibrium isotopic distribution by some post-formation process, proportions of clumped isotopologues could instead reflect chemical or physical kinetics, mixing, inheritance from a precursor, or so-called 'combinatorial' isotope effects (Yeung, 2016; Röckmann et al., 2016; Douglas et al., 2017; Stolper et al., 2018).

It has been argued that non-equilibrium methane clumped isotope abundances can be used to identify the mechanisms of microbial methanogenesis and methanotrophy, including the energetics and reversibility of metabolic reactions (Wang et al., 2015, 2016; Stolper et al., 2015; Gruen et al., 2018; Cao et al., 2019; Ash et al., 2019; Ono et al., 2021). Microbial methane can be produced by hydrogenotrophic and methylotrophic methanogenesis and consumed by methanotrophy through aerobic or anaerobic oxidation (Valentine et al., 2004; Valentine, 2011; Yoshinaga et al., 2014). These microbial metabolic processes can result in both equilibrated and non-equilibrated clumped isotope compositions in methane; both equilibrated and non-equilibrated compositions are common in natural environments, whereas all laboratory culture studies published to-date have produced non-equilibrium compositions (Wang et al., 2015; Stolper et al., 2015; Douglas et al., 2016; Young et al., 2017; Gruen et al., 2018; Giunta et al., 2019; Taenzer et al., 2020). Enzymatic reversibility has been proposed to control the expression of kinetic isotope effects during microbial methanogenesis. Specifically, the limitation of substrates in the deep subsurface and marine settings promotes reversibility of the elementary steps in methanogenesis and leads to equilibrated proportions of clumped isotopes of methane; whereas non-equilibrium compositions are observed in freshwater environments and laboratory cultures grown with high activities of substrates that drive rapid net methane formation (Valentine et al., 2004; Wang et al., 2015; Stolper et al., 2015). It has also been suggested that methane can be driven to internal isotopic equilibrium in marine sediments by anaerobic

oxidation (Ash et al., 2019). In that case, clumped isotope compositions record the temperature at which methane is oxidized rather than its initial production temperature (if different).

Abiotic methane can be produced by high-temperature reactions in the mantle or hydrothermal environments, as well as Fischer-Tropsch-Type (FTT) reactions (Etiope and Sherwood Lollar, 2013). Hydrothermal methane is thought to be produced in internal isotopic equilibrium in general, in which case its clumped isotope composition records its formation temperature (Wang et al., 2015, 2018; Douglas et al., 2017; Labidi et al., 2020); though some methane samples associated with hydrothermal vents are out of internal isotopic equilibrium and therefore suspected to be mixtures of microbial and abiotic gases (Young, 2019), or interpreted to be partially re-ordered at post-formation residence temperature (Labidi et al., 2020). In contrast, abiotic methane produced by laboratory Sabatier reaction and methane from crustal fluids that is interpreted to be abiotic and formed by FTT synthesis are both characterized by clumped isotope composition inconsistent with internal equilibrium; most notably, they exhibit pronounced deficits in $^{12}CH_2D_2$ compared to amounts expected for equilibrium at suspected gas generation temperatures, and in some cases compared to the stochastic distribution of all isotopes among all isotopologues (so-called 'anti-clumping' signatures). The non-equilibrated clumped isotope composition observed in the laboratory Sabatier reaction has been attributed to hydrogen quantum tunneling (Young et al., 2017), or 'combinatorial' isotope effect (Cao et al., 2019).

Thermogenic methane is generally recognized to form by catagenesis, or thermal 'cracking', of kerogen and other organic matter (Tissot and Welte, 1984). This process is generally considered irreversible, involving isotopic fractionations controlled by kinetic isotope effects (KIE) (e.g., Chung et al., 1988; Tang et al., 2000; Ni et al., 2011). However, the clumped isotope compositions of most thermogenic methane seem to be consistent with thermodynamic equilibrium at independently-constrained formation temperatures (D. A. Stolper et al., 2014; Wang et al., 2015; Young et al., 2017; Douglas et al., 2017; Stolper et al., 2018; Giunta et al., 2019). This discrepancy could be taken as evidence for an alternative hypothesis that catagenetic reactions proceed through locally reversible metastable equilibria (Helgeson et al., 2009; Mango et al., 2009; Thiagarajan et al., 2020b). Alternatively, like interpretations of some natural microbial methane, thermogenic methane might be produced by irreversible, kinetically controlled reactions, but subsequently driven to equilibrium by some more reversible chemical process. Regardless, this contradiction between common views of catagenesis and the implications of methane clumped isotope analyses presents a quandary.

Some insight to this issue comes from exceptional natural thermogenic methanes with apparent clumped-isotope temperatures that significantly disagree with independent constraints on their conditions of formation. Unconventional oil-associated gases are formed and stored within the same geologic formation (i.e., shale gases), and are associated with liquid hydrocarbons (i.e., methane is dissolved in a liquid hydrocarbon phase). The clumped-isotope-based temperatures of these gases exceed the expected maximum temperatures experienced by the associated oils, and in many cases do not represent feasible geological temperatures at which methane could co-exist with a liquid hydrocarbon phase; therefore they appear to have formed or been driven out of isotopic equilibrium (Douglas et al., 2017; Stolper et al., 2018). The disequilibria observed in those gases could reflect a chemical or physical kinetic isotope effect associated with the extraction of hydrocarbons (Stolper et al., 2018). Specifically, the recovery technique of

unconventional deposits is different from conventional reservoirs and requires hydraulic fracturing and production configurations that may impact the rate of gas desorption from the formation. Moreover, in the presence of liquid hydrocarbons, kinetic isotope effects could be expressed during dissolution/degassing of methane in/out of oil, diffusion from shale through hydraulic fractures, and adsorption or desorption onto shale. These effects are currently poorly understood and need to be examined by studying natural samples with known production histories and laboratory experiments.

Alternatively, the disequilibria in these natural thermogenic methanes could reflect chemical kinetic isotope effects in methane generation (Douglas et al., 2017; Stolper et al., 2018). Some support for this possibility comes from coal pyrolysis experiments, which generate methane with clumped-isotope compositions that are inconsistent with the experimental temperatures under some conditions (Shuai et al., 2018). In these experiments, the transition from equilibrated to non-equilibrated distributions of methane clumped isotopes coincide with the onset of ethane cracking. This finding was interpreted as evidence that methane generated from kerogen catagenesis forms in local isotopic equilibrium, but that methane formed by kinetically controlled cracking of alkyl moieties (ethane in particular) initially forms out of isotopic equilibrium (Shuai et al., 2018). Xia and Gao (2019) constructed a kinetic reaction network model to investigate the effect of kinetic isotopic fractionations on methane clumped isotopes during catagenesis. They predicted that 'anti-clumping' (marked clumped isotope deficits) can result from a 'combinatorial effect' in methane generation. Specifically, they argue that a combination of both a D-rich hydrogen pool and a D-poor hydrogen pool, or a combination of hydrogen atoms that experienced different deuterium KIE's, to the four hydrogens in the methane molecule leads to deficits in $^{12}CH_2D_2$ compared to the stochastic abundance. Additionally, no study to-date has resolved the relative contributions of the two doubly substituted isotopologues ($^{13}CH_3D$ and $^{12}CH_2D_2$) to the observed disequilibria (in Δ_{18}, combined clumped isotope index) in unconventional oil-associated methane and methane product in coal pyrolysis experiments (Douglas et al., 2017; Stolper et al., 2018; Shuai et al., 2018).

Here we report results of controlled pyrolysis experiments on n-octadecane ($C_{18}H_{38}$), focusing on measurements of both the $^{13}CH_3D$ and $^{12}CH_2D_2$ proportions in product methane, as well as the carbon and hydrogen isotope compositions of C_1-C_4 hydrocarbon products. We show that proportions of $^{13}CH_3D$ in product methane appear to be close to thermodynamic equilibrium at the temperatures of pyrolysis, or consistent with a random sampling of an apparently equilibrated or near equilibrated methyl group from the precursor(s), but that proportions of $^{12}CH_2D_2$ are strongly depleted relative to equilibrium at the experimental (or any) temperature. The distinctive depletion in $^{12}CH_2D_2$ associated with octadecane pyrolysis decreases in amplitude as pyrolysis proceeds, i.e., the composition of $^{12}CH_2D_2$ approaches equilibrium with maturation. We present a kinetic model to describe the behaviors of the five most abundant isotopologues of methane formed by octadecane pyrolysis. This model fits experimental results in all compositional properties we considered, and the fitted model parameters are consistent with independent constraints on isotope effects associated with carbon-carbon or carbon-hydrogen bond cleavage. The most important feature of the model is its explanation of the anomalous $^{12}CH_2D_2$ depletion as the result of a 'combinatorial effect' (Yeung, 2016; Röckmann et al., 2016; Xia and Gao, 2019), in this case attributable to the reaction of relatively deuterium-rich CH_3 radical intermediate with relatively deuterium-depleted capping hydrogen to form the product methane.

The subsequent approach to equilibrium with respect to $^{12}CH_2D_2$ abundance can be explained by hydrogen exchange reactions in the system. These experiments demonstrate that exceptional depletion in $^{12}CH_2D_2$ is not a unique signature of biosynthesis or Sabatier reactions, but also can result from thermally-induced methane generation. We propose a model of natural thermogenic methane generation that predicts the value of $\Delta^{12}CH_2D_2$ as a function of thermal maturation.

2. METHODS

2.1. Pyrolysis experiments

Aliquots of ~ 150 mg of n-octadecane (Alfa Aesar, LOT U28D017) were weighed and placed in quartz vessels. Each vessel is made of a bulb (1-inch outer diameter (OD), $1\frac{1}{4}$ inch long) joined to a 1/4-inch-OD, 7-inch-long tube. All parts of the vessel are made of 0.05-inch-thick quartz. The vessels were evacuated to approximately 10^{-4} Torr using a mercury diffusion pump backed by a rotary pump, while cooled to approximately 77 K by immersion in a liquid nitrogen bath, and then flame-sealed. Then, the sealed quartz vessels were placed in a Mellen NACCI tube furnace at 400°C and heated for 72 to 397 hours (Table 1).

The equivalent maturity (Easy%RoV) of each experiment was calculated using the experimental times and temperature following Sweeney and Burnham (1990) and Burnham (2019). Easy%Ro values calculated from Sweeney and Burnham (1990) were also provided (Table 1).

2.2. Recovery of experimental products

After pyrolysis, vessels were removed from the furnace and quenched within ~1 min to room temperature in air. The vessels were then opened using a tube cracker attached to a vacuum line. The gas product was expanded into an evacuated glass volume and split into two aliquots by closing a valve in the middle of the volume. Methane in one aliquot was purified following the method described in D.A. Stolper et al. (2014). C_{2+} hydrocarbons (and a small amount of methane and hydrogen gas) in the other aliquot were condensed into a Pyrex® tube by vapor transfer through a vacuum line, with the tube immersed in liquid nitrogen, and the tube was then flame-sealed for storage.

The amount of methane and the total gas product was measured by manometry and converted to molarity by the ideal gas law.

2.3. Compound-specific carbon and hydrogen isotope measurement

The $\delta^{13}C$ and δD of ethane, propane, propene, and n-butane of the recovered gas, and the starting substrate n-octadecane, were measured at Caltech by GC-combustion-IRMS (for $\delta^{13}C$) and GC-pyrolysis-IRMS (for δD) on a Thermo-Scientific Delta$^+$ XP. Gas products were introduced to a GS-GASPRO gas chromatography column (30m×0.320mm) through a programmed temperature vaporization (PTV) injector held at 160°C and operated in splitless mode, using He as a carrier gas flowing at 1.4 ml/min. The GC oven was held at 40°C for 5 min, and heated to 80°C, held for 3 min; then to 100°C, held for 4 min; and to 110°C, held for 9 min; and finally heated to 160°C, held for 8 min. All the ramping rates of temperatures were at 20°C/min. ~ 5 mg substrate

n-octadecane was dissolved in 1.5 ml hexane then diluted by 60 times. The solution was injected to a ZB-5MS column (30m×0.25mm×0.25μm film thickness) at a flow rate of 1.4 mL/min. The oven was started at 100˚C, and heated from 100˚C to 220˚C at 20˚C/min then to 240˚C at 5˚C/min and held for 3min. The PTV injector was in PTV Large Volume mode. The injector was held at 60˚C for 0.1min, then heated to 350˚C at 14.5˚C/sec and held for 1min before cooling down to 300˚C at 1˚C/sec. Co-injected peaks of methane reference gas (δD = -161.5‰) were used for single-point isotopic calibration of analytes. That reference gas was in turn calibrated against a standard solution of 8 fatty acid methyl esters ('F8 mix' of Arndt Schimmelmann, Indiana University). A working gas standard of C_2-C_5 gas mixture (including CIT-Ethane-1 and CIT-P1) is run along with the experimental samples to monitor instrumental status (Piasecki et al., 2016a; Clog et al., 2018; Xie et al., 2018).

$\delta^{13}C$ and δD are expressed using delta notation relative to Vienna Pee Dee Belemnite (VPDB) and Vienna Standard Mean Ocean Water (VSMOW), respectively:

$$\delta^{13}C = \frac{^{13}R_{sample}}{^{13}R_{VPDB}} - 1 \quad (1)$$

$$\delta D = \frac{^{D}R_{sample}}{^{D}R_{VSMOW}} - 1 \quad (2)$$

where $^{13}R = \frac{^{13}C}{^{12}C}$ and $^{D}R = \frac{D}{H}$; and $\delta^{13}C$ and δD values are reported in per mil notation. The long-term experimental reproducibility for measurements of standards and replicate samples on these instruments is 0.15‰ for $\delta^{13}C$ and 5‰ for δD (1SE).

The relative abundance of ethane, propane, and other hydrocarbons were calculated by the corresponding peak areas (reported by Isodat software of GC-combustion-IRMS) divided by the number of carbon atoms in each product molecule. A natural gas working standard with known relative concentrations for C_1-C_5 hydrocarbons (Table S1, characterized by Isotech Laboratories) is run to monitor relative sensitivities of compounds of interest.

The yield of each gas component was calculated as the mole ratio of carbon in that component to that of the carbon in starting material n-$C_{18}H_{38}$, e.g.:

$$yield_{methane} = \frac{molarity\ of\ carbon\ in\ the\ product\ methane}{molarity\ of\ carbon\ in\ the\ starting\ n-C_{18}H_{38}} \quad (3)$$

$$yield_{ethane} = \frac{molarity\ of\ carbon\ in\ the\ product\ ethane}{molarity\ of\ carbon\ in\ the\ starting\ n-C_{18}H_{38}} \quad (4)$$

2.4. Methane clumped isotope measurement

Values of $\delta^{13}C$ and δD and clumped-isotope compositions of methane were measured on a high-resolution isotope-ratio mass spectrometer, the Thermo Scientific Ultra, as described in detail by Thiagarajan et al., (2020), see also D.A. Stolper et al., (2014). Clumped-isotope compositions are expressed using $\Delta^{13}CH_3D$ and $\Delta^{12}CH_2D_2$ (D.A. Stolper et al., 2014) where

$$\Delta^{13}CH_3D = \frac{^{13}_{3}R}{^{13}_{3}R^{*}} - 1 \quad (5)$$

$$\Delta^{12}CH_2D_2 = \frac{^{12}_{2}R}{^{12}_{2}R^{*}} - 1 \quad (6)$$

and

$$^{13}CH_3D\,R = \frac{[^{13}CH_3D]}{[^{12}CH_4]} \quad (7)$$

$$^{12}CH_2D_2\,R = \frac{[^{12}CH_2D_2]}{[^{12}CH_4]} \quad (8)$$

The brackets denote the molar concentration of an isotopologue as a fraction of all methane molecules. R* is the ratio expected for a random (stochastic) distribution of isotopes amongst all isotopologues, based on the sample's δD and $\delta^{13}C$ values. Values obtained using Equations (5), and (6) are reported in per mil (‰). Δ values are converted into apparent temperature (in Kelvin) via the equations (Eldridge et al., 2019a):

$$\Delta^{13}CH_3D = \frac{1.47348 \times 10^{19}}{T^7} - \frac{2.08648 \times 10^{17}}{T^6} + \frac{1.19810 \times 10^{15}}{T^5} - \frac{3.54757 \times 10^{12}}{T^4} + \frac{5.54476 \times 10^{9}}{T^3} - \frac{3.49294 \times 10^{6}}{T^2} + \frac{8.89370 \times 10^{2}}{T} \quad (9)$$

$$\Delta^{12}CH_2D_2 = -\frac{9.67634 \times 10^{15}}{T^6} + \frac{1.71917 \times 10^{14}}{T^5} - \frac{1.24819 \times 10^{12}}{T^4} + \frac{4.30283 \times 10^{9}}{T^3} - \frac{4.48660 \times 10^{6}}{T^2} + \frac{1.86258 \times 10^{3}}{T} \quad (10)$$

2.5. Numerical modeling

We integrated ordinary differential equations in the numerical models presented in the discussion section of this study using MATLAB ordinary differential equation solver ODE15s. We found the best fits of models to experimental results using MATLAB nonlinear least-squares solver lsqcurvefit with the trust-region-reflective algorithm.

3. RESULTS

3.1. Gas chemistry

Methane, ethane, propane, propene, and n-butane are generated in all experiments (Fig. 1, Table 2). Ethene and hydrogen gas are also produced but not abundant enough to determine isotopic compositions. Ethane is the most abundant recovered gaseous component in all experiments (35-41% of bulk gas by molarity), whereas propene and n-butane are always trace components (≤ 6% of bulk gas by molarity). The gas remains quite 'wet' (i.e., rich in C_{2+} hydrocarbons) at all experimental durations, with $C_1/(C_2+C_3)$ of only 0.3 to 0.425. In the experiment with the longest duration, about 4% of carbon in starting n-octadecane is transferred to methane, 13% is transferred to ethane, and 12% to propane.

3.2. Compound-specific carbon and hydrogen isotope compositions of major gas products

The measured $\delta^{13}C$ and δD values of methane, ethane, propane, propene, and n-butane are given in Table 2 and Fig. 2. $\delta^{13}C$ and δD of methane evolved from -58.1 to -53.4‰ and from -309.2 to -250.2‰, respectively, as experimental duration progressed from 72 hours to 397 hours (Fig. 3a). Carbon and hydrogen isotope compositions of the other gas components all underwent similar increases with time throughout the experiments, maintaining an order of $\delta^{13}C$ and δD values: methane < ethane < propane < n-butane < propene.

The carbon isotope fractionation we observe between product methane and substrate n-octadecane approximately agrees (within 5%) with the previous experimental studies (Sackett, 1978; Jeffrey, 1981) and theoretical prediction of the KIE's associated with formation of methane from substrates n-hexane or n-octane (Tang et al., 2000; Xiao, 2001; Ni et al., 2011) (Table 4). However, for hydrogen isotopes, the observed methane—n-octadecane fractionation also agrees with previous experiments (Sackett, 1978), but is more extreme than that predicted by Tang et al. (2005) and Ni et al. (2011) (Table 4). We discuss this discrepancy in section 4.2.

3.3. Carbon and hydrogen isotope composition of the starting substrate n-octadecane

The $\delta^{13}C$ of n-octadecane is -32.9‰ and δD is -86‰ (Table 2, Fig. 2). Although we do not have clear information about the origin of the substrate from the supplier, this composition is consistent with that of petroleum materials (Schoell, 1984; Chung et al., 1992).

3.4. Clumped-isotope compositions of methane

The $\Delta^{13}CH_3D$ values of methane products are in the range of 0.2 to 1.9‰, which appear to be within 2-3 standard errors of the expected equilibrium composition of 1.2‰ at the experimental temperature (Table 2, Fig. 3b). However, the $\Delta^{12}CH_2D_2$ values span from -41 to -28‰, much lower than the equilibrium value of 2.0‰ at the experimental temperature and more variable than can be explained by analytical uncertainties alone (propagated 1 standard error 1.2-1.6‰). The $\Delta^{12}CH_2D_2$ values become less negative as the pyrolysis proceeds and equivalent thermal maturity (Easy%RoV) increases (Fig. 3b).

The $\Delta^{12}CH_2D_2$ values of methane produced in the pyrolysis of n-octadecane are among the lowest values observed in any prior study. Other comparable examples are abiotic methane produced by the Sabatier reaction in the laboratory (-55‰), microbial methane produced by methanogen cultures (-55 to -12‰) and from the boreal lake (-40‰), and natural gases from Southwest Ontario (-20 to -14‰) and the Michigan Basin (-23 to -11‰) (Young et al., 2017; Giunta et al., 2019; Gonzalez et al., 2019; Young, 2019). Previous findings of strongly negative $\Delta^{12}CH_2D_2$ values have been interpreted as evidence for KIE's (possibly including hydrogen tunneling effects) associated with low-temperature irreversible reactions; it is unexpected, in the context of prior interpretations of such anomalies, that similar signatures would be associated with pyrolytic reactions occurring at 400°C.

4. DISCUSSION

4.1. Kinetic isotope effects and compound-specific isotope compositions

The gas components produced from each experiment exhibit a negative linear correlation between $\delta^{13}C$ and 1/N, where N is the number of carbon atoms in each product molecule — the so-called 'Chung plot' (Fig. 4, Table 3). These trends conform to a model that explains carbon isotope compositions of natural gas components as a result of kinetic isotope effects associated with breaking a single carbon-carbon bond in a straight side chain from a larger precursor organic molecule (Chung et al., 1988). If one interprets the linear correlations in Fig. 4 in terms of this model, the vertical intercept is the $\delta^{13}C$ value of precursor organic molecule, whereas the slope represents the isotopic fractionation in bond breaking. However, the intercepts of trends defined by pyrolysis products of this study are higher in $\delta^{13}C$ than the starting substrate (Table 2, 3). It has been previously suggested that such discrepancies between the 'Chung diagram' intercepts and actual substrates reflect the fact that the precursor to gas components gets more enriched in heavy isotopes as reaction proceeds because of Rayleigh distillation (Rooney et al., 1995). This hypothesis could be supported by our observation that the 'Chung plot' intercepts generally increase as pyrolysis proceeds and methane yield increases. Alternatively, the evolution of these 'Chung plot' intercepts could be affected by secondary cracking of C_{2+} (Peterson et al., 2018). The slopes in Fig. 4 do not change systematically throughout the experimental period, presumably meaning the carbon isotopic fractionation associated with cracking reactions remains approximately constant at all experimental times. Additionally, the carbon isotope fractionations between C_1-C_4 and precursor octadecane are approximately consistent with theoretical predictions for homolytic cleavage on n-hexane and n-octane and β scission on n-octane (Tang et al., 2000; Xiao, 2001; Ni et al., 2011) (Table 4).

Notably, the $\delta^{13}C$ of propene does not follow the negative linear correlation defined by most C_1 to C_4 species in Fig. 4 (see also Table 2). Instead, propene $\delta^{13}C$ is higher than expected by such observed correlation and even higher than that of the starting n-octadecane. We speculate that the distinctive ^{13}C enrichment of propene reflects an inverse KIE (i.e., a faster net reaction for heavy isotopologues) that results from β-scission of a radical precursor to yield an alkene, for example,

$$CH_3CH_2CH_2\dot{C}HCH_3 \Leftrightarrow CH_3\dot{C}H_2 + CH_2{=}CHCH_3 \quad \text{(R3)}$$

where a new double bond is formed to the central carbon in propene. Reaction (R3) is predicted to have a product-like transition state, i.e., the transition state is late and has some of the character of the double bond in product propene (Jitariu et al., 2003). Therefore, the carbon destined for the central site of propene will experience a more confined bonding environment in the transition state than in the reactant. Transition state theory predicts the kinetic isotope effect of reaction (R3) to be the equilibrium isotope fractionation between the transition state and the reactant, which leads to an inverse kinetic isotope effect (Bigeleisen and Wolfsberg, 1957). Similarly, we note that propene also has a higher δD than the starting n-octadecane. We suspect the deuterium enrichment in propene sources from its radical precursor, where the radical precursor experiences hydrogen isotope fractionation in isomerization, for example,

$$CH_3CH_2CH_2CH_2\dot{C}H_2 \Leftrightarrow CH_3CH_2CH_2\dot{C}HCH_3 \quad \text{(R4)}$$

where an inverse secondary KIE may result from the change of orbital hybridization on the terminal carbon from sp^2 to sp^3 (e.g., Singleton and Thomas, 1995). Alternatively, secondary cracking of propene and its conversion to graphitic products may contribute to the enrichment of ^{13}C and D in the residual propene. Additionally, alkene and alkane can attain metastable

equilibrium in their relative abundance in hundreds of hours in the presence of H_2 under hydrothermal conditions (Seewald, 1994). If propene and propane are also in isotopic equilibrium, we might expect higher $\delta^{13}C$ and δD of propene than propane in the experiments (Table 2). We are not aware of any first-principles theoretical studies of the carbon or hydrogen isotopic fractionations associated with propene generation by β-scission or equilibrium fractionation between propene and propane, but such studies would be obvious ways to further explore these hypotheses.

The hydrogen isotope fractionation between wet gases (C_2 to C_4) and precursor octadecane has an order of ethane > propane > n-butane. Following the logic of common interpretations of the Chung diagram (above), this order could reflect the proportions of hydrogen that was isotopically fractionated by secondary KIE's in carbon-carbon bond cleavage as a fraction of all hydrogen in the product molecule, i.e., relatively more hydrogen sites in ethane are fractionated than those in propane, than those in n-butane. However, the hydrogen isotope fractionations between wet gases and source substrate octadecane are 30-150‰ more negative than those predicted by Ni et al. (2011) (Table 4). We suggest this discrepancy could have the same origin(s) as the discrepancy between predicted and experimental results of methane-octadecane fractionations, as stated in 3.2. We return to this issue in more detail in 4.2.1 and 4.2.2.4.

The chemical and isotopic compositions of C_2 to C_4 gases in our experiments offer insights into the reactions by which they formed and are relevant to the interpretation of the isotopic composition of product methane, which we develop in detail below. However, the depth of analysis required to fully address the findings for wet gas compounds goes beyond the scope of this paper and will be addressed in a future paper.

4.2. Modeling the isotopic content of methane in pyrolysis of n-octadecane

We propose a model of the reactions and accompanying isotopic fractionations associated with methane formation by alkane cracking as an aid to understanding and quantifying the isotopic content of methane in the pyrolysis experiments of n-octadecane. Any such model should address the following features of our experimental results: values of $\Delta^{12}CH_2D_2$ of product methane that reach negative tens of per mil; ~-200‰ fractionation between δD of product methane and precursor n-octadecane; and a trend of increasing $\delta^{13}C$, δD, and $\Delta^{12}CH_2D_2$ of methane with time and progress of pyrolysis reactions (Fig. 3). We present two separate models that attempt to quantitatively explain these data. Both can explain the depleted $\Delta^{12}CH_2D_2$ and δD values of product methane, but the first — a model of cracking reactions alone — is incapable of describing the rise of $\Delta^{12}CH_2D_2$ with time and the rate of increase in δD with time for methane, whereas the second — a coupled model of cracking reactions and hydrogen exchange of product methane — captures those features. We present the cracking model first despite its inadequacy to fully fit the experimental results because its discussion demonstrates the kinetic isotope effects in methane generation and the 'combinatorial effect', which are also key components of our more successful and complex second model. We then add hydrogen exchange reactions to the cracking model, thereby explaining all major features of the experimental data.

4.2.1. Cracking model

4.2.1.1. methane formation and 'capping' hydrogen

Pyrolytic chemistry, or 'cracking', of n-alkanes involves different types of elementary reactions. Cracking can initiate with a family of homolytic cleavage reactions on different carbon-carbon bonds of n-alkanes. Various alkyl radical intermediates can (1) go through further cracking through β scission reactions, producing alkene and alkyl radical, (2) rearrange the position of the single electron in the radical structure by alkyl isomerization, or (3) transform to a neutral, stable product by hydrogen abstraction. The stable product can experience further cracking in the same manner as the starting n-alkane. Such a reaction network involves alkanes, alkenes, and alkyls of various carbon numbers. Therefore, a chemical kinetic model of pyrolysis often incorporates hundreds of chemical species and thousands of reactions (e.g., Yi et al., 2011; Wang et al., 2017). Alternatively, previous studies have developed kinetic models for oil cracking and natural gas generation with overall reactions from stable precursors to stable products and/or using generalized compound classes to represent complex mixtures (Ungerer et al., 1988; Jackśon et al., 1995; Tang et al., 2000).

Methane formation in pyrolysis of n-alkane involves breaking a carbon-carbon bond through homolytic cleavage or β-scission of hydrocarbon precursors, creating a methyl radical as an immediate product (Fig. 5). This radical is metastable and short-lived, transforming to a neutral, stable methane molecule by abstracting a hydrogen radical that 'caps' the single electron in the methyl-radical intermediate (Fig. 5). The KIEs in such a process of methane generation include a primary ^{13}C KIE and a secondary deuterium KIE in breaking the carbon-carbon bond, and a primary deuterium KIE in breaking a carbon-hydrogen bond when abstracting the 'capping' hydrogen. A primary deuterium KIE in hydrogen abstraction by a methyl radical can be as large as ~ -700‰ at 400°C (Gray et al., 1971). However, isotope effects associated with extracting the capping hydrogen from its precursor(s) have long been ignored in theoretical studies on compound-specific hydrogen isotope compositions of natural gas (e.g., Ni et al., 2011), until recently Xia and Gao (2019) showed such a primary deuterium KIE may affect clumped isotope composition of methane.

4.2.1.2. Cracking model setup

In order to test the effect of capping hydrogen on the isotopic content of methane produced in pyrolysis experiments, we consider the following methane generation reaction in n-octadecane pyrolysis:

$A\text{-}CH_3 + B\text{-}H \rightarrow A\cdot + B\cdot + CH_4$ (R5)

where $A\text{-}CH_3$ represents methyl precursors and B-H represents hydrogen bearing compounds (Xia and Gao, 2019). The reaction rate of (R3) is:

$$\frac{d[CH_4]}{dt} = k_{CH4Gen}[ACH_3][BH] \quad (11)$$

where [i] represents the concentration of species i and k_{CH4Gen} is the rate constant of (R5). We model the generation of the five most abundant isotopologues of methane numerically with 14 isotopic species and 8 isotope-specific reactions (RA1-RA8 in Table A1). We incorporate the primary ^{13}C KIE for $A\text{-}^{13}CH_3$ ($^{13C}KIE_{PRI}$), secondary deuterium KIE for $A\text{-}^{12}CH_2D$ ($^{D}KIE_{SEC}$), and primary deuterium KIE for B-D ($^{D}KIE_{PRI}$) on the rate constants of these reactions (Table A1, Appendix A1). We assume the kinetic isotope effect for multiply-substituted species is the product of the KIE's for the corresponding singly-substituted species (as would occur in the case

of no clumped-isotope-specific kinetic isotope effects). This approximation is reasonable because clumped-isotope-specific chemical kinetic vibrational isotope effects in this system at 400°C are expected to be much smaller than the $^{12}CH_2D_2$ anomaly we wish to explain. All concentrations in the model are normalized by moles of starting n-octadecane in the experiments. The initial concentration of A-CH_3 is constrained by the rate of increase in methane $\delta^{13}C$ (i.e., the slope of Fig. 6a is determined by the size of the A-CH_3 pool that experiences Rayleigh distillation), and is consistent with the number of methyl groups in n-$C_{18}H_{38}$. The initial concentration of B-H is constrained by the number of hydrogen atoms in n-$C_{18}H_{38}$ excepting methyl groups (Table 5). The rate constant for $^{12}CH_4$ generation (k_{CH4Gen}) is fitted to the time evolution of the yield of methane (Fig. 1a) with methods described in section 2.5. We use the measured $\delta^{13}C$ and δD values of n-$C_{18}H_{38}$ to set the D/H and $^{13}C/^{12}C$ ratios of A-CH_3 and B-H. And we fit $^{13C}KIE_{PRI}$, $^{D}KIE_{PRI}$, $^{D}KIE_{SEC}$ and initial clumped isotope compositions of the methyl group in A-CH_3 ($\Delta^{13}CH_2D$ and $\Delta^{12}CHD_2$) to the measured time evolutions in isotopic properties of methane using methods detailed in section 2.5 (Table 5).

4.2.1.3. Rayleigh distillations and the combinatorial effect

We find the cracking model fits the time evolution of the yield and $\delta^{13}C$ of methane with an R^2 of 0.73 and 0.71 (Fig. 1a, Fig. 6a), and fits measured $\Delta^{13}CH_3D$ values to within 2 standard errors (Fig. 6d). However, this model fits δD and $\Delta^{12}CH_2D_2$ poorly with R^2 of 0.30 and -0.29, respectively (Fig. 6b, c).

The modeled increase in $\delta^{13}C$ and δD with time reflects the fact that the isotopic compositions of the accumulated products of Rayleigh distillation trend toward that of the source substrate as reaction proceeds (Fig. 6a, b). The enrichment of $\delta^{13}C$ of product methane with time agrees well with the modeled trend, however, the increase in methane δD in experiments is more rapid than that expected for the effect of Rayleigh distillation during cracking (Fig. 6b, see also Fig. A1).

The $\Delta^{12}CH_2D_2$ value of methane produced by cracking are modeled to be 30-40‰ lower than the stochastic distribution (Fig. 6c). In the cracking model, product methane inherits three out of its four hydrogen atoms from the methyl precursor (A-CH_3) with a fitted KIE of ~0.928 (Table 5), leading to a δD value of ~ -150‰. The fourth hydrogen in the product methane, the capping hydrogen, is abstracted from hydrogen bearing compound (B-H) with a fitted KIE of ~0.357 (Table 5), resulting in a δD value for this capping hydrogen as low as ~ -670‰. Therefore, the three hydrogen atoms from A-CH_3 in each methane molecule constitute a pool with higher deuterium concentration, $[D]_A$, whereas the capping hydrogen from BH makes up a second pool with lower deuterium concentration, $[D]_B$, the deuterium concentration of product methane is the weighted average of these two pools:

$$[D]_{CH4} = (3[D]_A + [D]_B)/4 \quad (12)$$

Nevertheless, the four hydrogen atoms are symmetrically equivalent in a product methane molecule. This symmetric equivalence leads one to predict a stochastic abundance of $^{12}CH_2D_2$ (the reference frame for $\Delta^{12}CH_2D_2$ values) as

$$[^{12}CH_2D_2]_{sto} \approx 6\times[D]_{CH4}\times[D]_{CH4} = 6\times[(3[D]_A + [D]_B)/4]^2 \quad (13)$$

However, the actual probability of randomly forming $^{12}CH_2D_2$ is:

$$[^{12}CH_2D_2] \approx 3\times[D]_A\times[D]_B + 3\times[D]_A^2 \quad (14)$$

And for all cases where $[D]_A$ and $[D]_B$ lie between 0 and 1 and are unequal:

$6\times[(3[D]_A+[D]_B)/4]^2>3\times[D]_A\times[D]_B+3\times[D]_A^2$ (15)
This inequality in (15) leads to negative $\Delta^{12}CH_2D_2$ (i.e., deficit relative to stochastic distribution). And larger differences between $[D]_A$ and $[D]_B$ lead to larger deficits in $\Delta^{12}CH_2D_2$ (Fig. A1). Note that we leave out the [H] terms in the derivation above (though it is included in the numerical model) to make the inequality easier to prove. This approximation leads to no analytically resolvable systematic errors provided $0<[D]_A<0.001$ and $0<[D]_B<0.001$ (i.e., when δD of both pools is < ~5400‰ — clearly true in the case of our experiments).

This mechanism for producing exceptional clumped isotope Δ values has been called the 'combinatorial effect' (Yeung, 2016; Röckmann et al., 2016; Clog et al., 2018; Cao et al., 2019; Xia and Gao, 2019; Taenzer et al., 2020). Such effects can arise any time two or more symmetrically equivalent molecular sites are created in such a way that they have different probabilities of containing a rare isotope substitution; these anomalies have been observed in microbial methane (Taenzer et al., 2020), and predicted for O_2, N_2 (Yeung, 2016) and ethane (Clog et al., 2018), and should be expected for emerging clumped isotope systems like sulfate (Ueno et al., 2019; Neubauer et al., 2020), H_2 (Popa et al., 2019), perchlorate (Martin, 2020), nitrate (Neubauer et al., 2020), and Δ_{48} in CO_2 (Fiebig et al., 2019a; Bajnai et al., 2020).

The cracking model predicts a 5‰ decrease in $\Delta^{12}CH_2D_2$ over the course of experiments (Fig. 6c). This reflects the fact that B-H is a larger reservoir for capping hydrogen than A-CH_3 is as a reservoir for methyl. So the increase in δD of residual B-H caused by Rayleigh distillation is smaller than that for residual A-CH_3. This effect reinforces the difference in δD between the methyl group and capping hydrogen, and the modeled $\Delta^{12}CH_2D_2$ value decreases further with experimental time rather than increases as we observe.

No combinatorial effect is expected for the $\Delta^{13}CH_3D$ value in the model. The stochastic abundance of $^{13}CH_3D$ is
$[^{13}CH_3D]_{sto}\approx 4\times[^{13}C]_{CH4}\times[D]_{CH4}=[^{13}C]_{CH4}\times(3[D]_A+[D]_B)$ (16)
In the model, $^{13}CH_3D$ forms by inheriting its ^{13}C from A-CH_3, whereas the deuterium may be inherited either from A-CH_3 or B-H (Table A1). The probability of randomly forming $^{13}CH_3D$ is
$[^{13}CH_3D]\approx[^{13}C]_A\times3\times[D]_A+[^{13}C]_A\times[D]_B$ (17)
And (16)=(17).

The 0.5‰ decrease in modeled $\Delta^{13}CH_3D$ value over the course of experiments (Fig. 6d) reflects a nonlinear effect of producing methane from a progressively fractionated precursor pool (A-CH_3) in a Rayleigh distillation process. This stems from clumped isotope mixing effects — when one mixing endmember has higher $\delta^{13}C$ and δD than the other endmember, the nonlinear variations in $\Delta^{13}CH_3D$ of the mixture will lead to a positive anomaly (Douglas et al., 2016). In our model, the initial methyl precursor (A-CH_3) separates into a product pool that experiences KIEs and therefore has depleted $\delta^{13}C$ and δD, and a residual reactant pool that experiences enrichment in $\delta^{13}C$ and δD. Following the nonlinearity of mixing in Δ values, the initial precursor will have a higher $\Delta^{13}CH_2D$ value than the weighted average of those of the product pool and the residual reactant pool. Since the product has the same $\Delta^{13}CH_2D$ value as the initial precursor (because of no clumped-isotope-specific KIEs), the residual reactant will have lower $\Delta^{13}CH_2D$ than the initial precursor. As the reaction proceeds, $\Delta^{13}CH_2D$ of the residual reactant gradually decreases, following a trend of Rayleigh distillation. Therefore, it causes $\Delta^{13}CH_3D$ of

product methane to decrease in the cracking model — but only subtly (by less than 2 standard errors of measurement; Fig. 6d).

4.2.1.4. Summary of cracking model

The cracking model demonstrates that the combinatorial effect of combining methyl and the 'capping' hydrogen leads to the large deficit in $\Delta^{12}CH_2D_2$ (Fig. 6c, A1) and draws down the δD of product methane (eqn. (12), Fig. A1) — both noticeable features of our experimental products. Nevertheless, this model is incapable of capturing the time-evolving enrichments of δD and $\Delta^{12}CH_2D_2$ as pyrolysis proceeds. Consequently, as we consider these enrichments a robust observation (both trends have amplitudes that exceed 10 standard errors of measurements), we develop a model that considers additional chemical reactions with the purpose of explaining these observations.

4.2.2. Cracking-exchange model

In this section, we develop a model that can explain the rate of enrichment in $\delta^{13}C$, δD, and $\Delta^{12}CH_2D_2$ and lack of analytically significant change in $\Delta^{13}CH_3D$ with pyrolysis progress (Fig. 3). The increase of $\delta^{13}C$, δD, and $\Delta^{12}CH_2D_2$ with thermal maturity (Ro) has also been observed in natural gases (Xie et al., 2019), so understanding this feature of our experimental results may be significant for the interpretation of data for natural samples.

4.2.2.1. hydrogen exchange reactions

The relatively rapid rise in δD and $\Delta^{12}CH_2D_2$ of methane in our experiments could reflect several processes, but we focus our attention on hydrogen exchange because it is known to be an important process both in pyrolysis experiments and in nature (Sessions et al., 2004; Schimmelmann et al., 2006; Sessions, 2016; Wei et al., 2019; Labidi et al., 2020; Xie et al., 2020).

Methane might exchange hydrogen during the pyrolysis with any of the co-existing hydrogen bearing compounds, i.e. hydrocarbons including precursor n-octadecane. However, we are not aware of experimental or theoretical constraints on the kinetics of hydrogen exchange between hydrocarbon compounds in absence of metal catalyst. This should be investigated in future research. Our best constraint on the rates of hydrogen exchange involving methane is perhaps its exchange with water, as water is a plausible substrate participating in hydrogen exchange in sedimentary environments (Sessions et al., 2004; Schimmelmann et al., 2006; Sessions, 2016). The half-life for hydrogen exchange between methane and water has been estimated to be on the time scale of tens of hours to a year at the temperature of our pyrolysis experiments, and millions of years in sedimentary basins (Wang et al., 2018 and references herein). Although the chemical mechanism of hydrogen exchange can be different for specific types of reactions (free-radical reactions versus reactions involving carbonium ions), the time scale of equilibration through hydrogen exchange observed in these previous studies seems broadly consistent with that of our pyrolysis experiments and natural gas formation at corresponding temperatures.

4.2.2.2. Cracking-exchange model setup

In order to test the effect of hydrogen exchange on the isotopic composition of methane produced in pyrolysis experiments, we add to the cracking model in 4.2.1 (1) hydrogen exchange reactions between the five most abundant isotopologues of methane and hydrogen bearing compound B-H or B-D

$CH_xD_y + B\text{-}H \rightleftarrows CH_{x+1}D_{y-1} + B\text{-}D$ (R6)

where CH_xD_y and $CH_{x+1}D_{y-1}$ represent isotopologues of methane participating in the exchange, and (2) hydrogen exchange reactions among the five most abundant isotopologues of methane, via (R1) and (R2) (see a full list of exchange reactions in Table A1). The rate of each methane-BH or methane-methane exchange reaction is:

$r_n = \sigma_r\, k[i][j]$ (11)

where r_n is the rate of reaction RAn (n = 9-20) in Table A1, σ_r and k are the symmetry number and the rate constant of RAn, respectively, and [i] and [j] are concentrations of reactants of RAn (Table A1, Appendix A1).

We develop a cracking-exchange model numerically with 14 isotopic species and 20 isotope-specific reactions (Table A1). In addition to the parameters in the cracking model, we incorporate a primary ^{13}C KIE for exchange involving $^{13}CH_4$ ($^{13C}KIE_{PRI}^{C\text{-}H}$), a secondary deuterium KIE for exchange involving $^{12}CH_3D$ ($^{D}KIE_{SEC}^{C\text{-}H}$), an equilibrium hydrogen isotope fractionation between methane and BH ($^{D}\alpha^{eq}_{CH4\text{-}BH}$), and equilibrium constants of reaction (R1) (K_{13CH3D}) and (R2) ($K_{12CH2D2}$) (Eldridge et al., 2019a) in the rate constants of these reactions (Table A1, Appendix A1). We assume the kinetic isotope effect for multiply-substituted species is the product of corresponding singly-substituted species, as in the cracking model. All concentrations in the model are normalized by moles of starting n-octadecane in experiments.

The initial concentrations of A-CH_3 and B-H, and the rate constant for $^{12}CH_4$ generation (k_{CH4Gen}) are the same as in the cracking model because hydrogen exchange reactions do not alter the molecular compositions of methyl precursors (A-CH_3), hydrogen bearing compounds (B-H) or methane. We use the measured $\delta^{13}C$ and δD values of n-$C_{18}H_{38}$ to set the D/H and $^{13}C/^{12}C$ ratios of A-CH_3 and B-H. And we fit $^{13C}KIE_{PRI}$, $^{13C}KIE_{PRI}^{C\text{-}H}$, $^{D}KIE_{PRI}$, $^{D}KIE_{SEC}$, $^{D}KIE_{SEC}^{C\text{-}H}$, $^{D}\alpha^{eq}_{CH4\text{-}BH}$, the initial clumped isotope compositions of the methyl group in A-CH_3 ($\Delta^{13}CH_2D$ and $\Delta^{12}CHD_2$) and the rate constants of the methane-BH hydrogen exchange reaction ($k_{CH4\text{-}BH}$) and the methane-methane hydrogen exchange reaction ($k_{CH4\text{-}CH4}$), where the fit minimized disagreement with time evolution of all measured isotopic properties of methane using methods given in section 2.5 (Table 5).

4.2.2.3. Partial equilibration of δD and $\Delta^{12}CH_2D_2$ in the cracking-exchange model

We find the cracking-exchange model fits the time evolution of yield, $\delta^{13}C$, δD and $\Delta^{12}CH_2D_2$ of methane with an R^2 of 0.73, 0.71, 0.87, and 0.58 (Fig. 1, Fig. 7a, b, c), and fits the $\Delta^{13}CH_3D$ values to within 2 to 3 standard errors (Fig. 7d). We conclude this model is capable of simultaneously describing all major features of the experimental data.

In contrast to the cracking model, δD and $\Delta^{12}CH_2D_2$ of methane in the cracking-exchange model increase at a rate consistent with experimental results (Fig. 7b, c). This reflects the fact that hydrogen exchange reactions between methane and co-existing hydrogen bearing compound B-H

partially equilibrates the hydrogen isotope fractionation between methane and BH throughout our experimental period. This equilibration process leads to an increase in δD of methane with time more rapid than that expected for Rayleigh distillation alone (Fig. 6b, 7b). The half-life of methane δD equilibration is 415 hours in the model (if approximated as a pseudo first-order reaction). This process also partially equilibrates clumped isotope compositions of methane as it affects all of methane's hydrogen atoms equally, and therefore partially erases the $\Delta^{12}CH_2D_2$ deficit (Fig. 7c).

The experimental data are consistent with the cracking-exchange model results, with or without methane-methane hydrogen exchange reactions using our fitted parameters (Fig. S1). This may reflect the fact that the hydrogen exchange between methane and other hydrogen bearing compounds (B-H) is more important to the equilibration of $\Delta^{12}CH_2D_2$ in the experiments than methane-methane hydrogen exchange reactions.

The modeled $\Delta^{13}CH_3D$ value decreases by ~ 2‰ over the course of our experiments (Fig. 7d). This decrease results from the nonlinear effect of Rayleigh distillation (4.2.1.3) and hydrogen exchange reactions (Xia and Gao, 2019). Specifically, the primary ^{13}C KIE in breaking the carbon-hydrogen bond of methane in reactions (RA11) and (RA14) slows down the equilibration of $^{13}CH_3D$. This trend is not clearly evidenced by our data, but could be consistent with observations, given analytical uncertainties.

4.2.2.4. Model assumptions and comparison of fitted parameters with prior constraints

In the model, we assume the isotopic compositions of A-CH_3 and B-H are equal to $\delta^{13}C$ and δD values of n-$C_{18}H_{38}$ measured by GC-combustion/pyrolysis-irMS, i.e., the average values for all carbon and hydrogen sites in n-$C_{18}H_{38}$. So any difference in isotopic composition between the precursors of methyl groups (A-CH_3), precursors of capping hydrogens (B-H), and the rest of the sites of the substrate will be interpreted as contributing to the net KIE observed in the reaction. In a potentially extreme case that A-CH_3 and B-H have different δD values of -85.7 and -572.0‰, respectively (one of the largest measured intramolecular hydrogen isotope contrast in fatty acids from plants (Billault et al., 2001)), and assuming product methane inherits hydrogen atoms without any KIEs, we predict a deficit of -23‰ in $\Delta^{12}CH_2D_2$ and hydrogen isotope fractionation between methane and starting A-CH_3 of -133‰. We do not know the site-specific hydrogen isotopic composition of our reactant n-octadecane, so its contribution to the deficit in $\Delta^{12}CH_2D_2$ cannot be quantified (in fact, we are not aware of any measurements of natural-abundance, site-specific hydrogen isotope structures of alkanes larger than propane). But this problem should be revisited if and when it becomes possible to directly couple clumped isotope measurements of product methane with site-specific measurements of the D/H ratios of alkyl and methyl groups from methane's precursor.

The primary and secondary KIEs of breaking carbon-carbon and carbon-hydrogen bonds in n-alkanes through homolytic cleavage, β scission and hydrogen abstraction have been systematically studied with density function theory calculations (Canadell and Olivella, 1984; Lu et al., 1990; Tang et al., 2000, 2005; Xiao, 2001; Ni et al., 2011), or laboratory experiments (Jackson et al., 1962; Gray et al., 1971 and references herein). The values we fit for the KIEs of

both carbon and hydrogen isotopes in the cracking-exchange model are within 10% of previous predictions and experimental results (Table 5). We conclude that the fitted KIEs are consistent with the range of these independent constraints.

Gray et al. (1971) noted that the experimentally-determined KIE's (k_D/k_H) for a series of hydrogen abstraction reactions by methyl radicals are smaller than predicted. At the temperature of our experiment (400°C), experimental primary deuterium KIE's are ~ 100-150‰ lower than predictions. These predictions assume the C-H stretching mode of the abstracted hydrogen is lost in the transition state (i.e., the stretching frequency becomes imaginary). Gray et al. proposed two hypotheses to explain the contradiction between experimental and predicted KIEs: first, in addition to the stretching mode, the bending mode may also be lost in the transition state. This change leads to a prediction in better agreement with the experimental value. A second possible explanation for the lower kinetic isotope effect is caused by quantum mechanical tunneling of hydrogen. However, previous calculations do not show significant tunneling contributions to the KIE in methyl radical attacking a methylene or methyl group (Johnston and Rapp, 1961; Salomon, 1964; Gray et al., 1971). In any case, we note that our fitted model is consistent with the experimental constraints on the KIE in hydrogen abstraction.

The equilibrium hydrogen isotope fractionation between methane and hydrogen-bearing alkyl compound B-H ($^{D}\alpha^{eq}_{CH4\text{-}BH}$) at 400°C can be estimated from reduced partition function ratios using Urey-Bigeleisen-Meyer (U-B-M) theory, with reduced partition functions extrapolated to our experimental temperature (Wang et al., 2009) or calculated from vibrational frequencies of fundamental modes computed by density function theory (Piasecki et al., 2016b). The fitted $^{D}\alpha^{eq}_{CH4\text{-}BH}$ value in our model is consistent with these estimated constraints within 2-3 standard errors of δD measurement by GC-pyrolysis-irMS (Table 5).

We are not aware of any published experimental studies that characterize the clumped isotope compositions of methyl groups in hydrocarbon compounds, or any computational studies on isotopic clumping in methyl in compounds larger than ethane. Nonetheless, the equilibrium $\Delta^{13}CH_2D$ and $\Delta^{12}CHD_2$ of the methyl group in ethane can be calculated using U-B-M reduced partition function theory (Piasecki et al., 2016b). The equilibrium $\Delta^{13}CH_2D$ and $\Delta^{12}CHD_2$ values are predicted to be 1.068‰ and 1.853‰ at 400°C, respectively. In our cracking model, the fitted initial clumped isotope compositions of methyl groups are within 2 standard errors of $\Delta^{13}CH_3D$ and $\Delta^{12}CH_2D_2$ measurements (Table 5). In the cracking-exchange model, the fitted initial $\Delta^{13}CH_2D$ and $\Delta^{12}CHD_2$ are 3.02‰ and 0.07‰, respectively. Sensitivity tests of our model show that $\Delta^{13}CH_3D$ is sensitive to the initial $\Delta^{13}CH_2D$ of the methyl group, which agrees with the findings in Xia and Gao (2019). Nevertheless, for the highly-depleted $\Delta^{12}CH_2D_2$ values observed in our experiments, any initial $\Delta^{12}CHD_2$ value in a plausible range (0-8‰) does not significantly affect the modeled $\Delta^{12}CH_2D_2$ value.

While the $\Delta^{13}CH_3D$ values of experimental products appear to be consistent with the thermodynamic equilibrium composition at 400°C, within two standard errors, we recognize that this does not necessarily indicate that $^{13}CH_3D$ forms in or conforms to thermodynamic equilibrium throughout the experimental period. In fact, our model predicts that methane initially inherits the $\Delta^{13}CH_2D$ of the methyl precursor, and both the generation and subsequent hydrogen exchange reactions can have kinetic effects on $\Delta^{13}CH_3D$ (Fig. 6d, 4.2.1.3, Fig. 7d, 4.2.2.3).

Although the range of our experimental data constrains that such kinetic effects on $\Delta^{13}CH_3D$ values are limited throughout the experimental period, these kinetic effects in Rayleigh distillation and exchange reactions may be able to explain the non-equilibrated and, in some cases, negative Δ_{18} values of methane produced during pyrolysis of coal (Shuai et al., 2018; Xia and Gao, 2019).

A recent non-peer-reviewed presentation reports isotopic contents of methane produced by the high temperature (600°C) pyrolysis of an ethane substrate, finding results broadly similar to those reported here (i.e., apparently equilibrated $\Delta^{13}CH_3D$ and highly-depleted $\Delta^{12}CH_2D_2$ values; Eldridge et al., 2019b). It has also been shown recently that low-temperature *Pseudomonas stutzeri* cultures produce methane by combining a methyl group (formed by decomposing methylphosphonate, CH_3O_3P) and a hydrogen atom from water (Taenzer et al., 2020). The combinatorial effect can explain the observed $\Delta^{13}CH_3D$ and $\Delta^{12}CH_2D_2$ values and is particularly clearly evidenced by variation of $\Delta^{12}CH_2D_2$ between methane formed in the presence of waters of various hydrogen isotope compositions. In that study, $\Delta^{13}CH_3D$ values are invariant in a range of -0.3 to 0.93‰ — similar to those observed here and by Eldridge et al. (2019b), but out of equilibrium at culture temperature. While the role of combinatorial effects on $^{12}CH_2D_2$ seems clear in all of these studies, further insight into the controls of $^{13}CH_3D$ will require investigations of the clumped isotope composition of methyl groups in the precursors of methane (i.e., n-octadecane, ethane, and methylphosphonate in the studies discussed above), as well as further understanding of the kinetics of hydrogen exchange reactions.

4.3. Modeling the isotopic content of natural thermogenic methane

We extrapolate the cracking-exchange model to geological times and temperatures to test whether the processes we propose that controlled our experiments might also explain the known patterns of isotopic variation associated with the production of thermogenic methane. The aim of this modeling activity is not to provide fitted parameters universally applicable to thermogenic methane formation, nor to assert that the chemistry of our experiments must necessarily be relevant to natural thermogenesis; rather, we ask whether adapting the cracking-exchange model to data of natural thermogenic methane will lead to a plausible and testable mechanistic hypothesis that explains its observed isotopic properties, which are generally open to a range of interpretations (D. A. Stolper et al., 2014; Young et al., 2017; Stolper et al., 2018; Giunta et al., 2019; Xia and Gao, 2019).

We can predict the isotopic properties of methane if it forms by the mechanisms included in the model of our experiments, and the kinetics of the model follow the Arrhenius equation and experience kinetic isotope effects on the pre-exponential factors and activation energies (Gray et al., 1971; Tang et al., 2000; Ni et al., 2011; Xia and Gao, 2019). We impose a temperature-time history where the temperature range and the heating rate simulate the process of typical sedimentary burial (Table 6). A full description of the model setup is in Appendix A2.

For equivalent thermal maturity (Easy%RoV, Burnham, 2019) between 0.6 and 0.8, our model predicts that this low-maturity thermogenic methane will have $\delta^{13}C$ of −65~ −50‰ and δD of −440 ~ −300‰. Both $\delta^{13}C$ and δD are expected to then increase with subsequent maturation until δD reaches equilibrium with co-existing hydrogen-bearing compounds at Easy%RoV ~ 1.5 (Fig.

8a). $\Delta^{12}CH_2D_2$ of low-maturity methane is predicted to start as low as ~ -60‰ because of the combinatorial effect, then rise to partially equilibrated $\Delta^{12}CH_2D_2$ values of -25 ~ 0‰ for maturities in the range of Easy%RoV ~0.8-1.2, and finally reach equilibrated $\Delta^{12}CH_2D_2$ values at maturity Easy%RoV > ~1.2 (Fig. 8b, c). The $\Delta^{13}CH_3D$ composition is predicted to decrease relative to substrates when Easy%RoV < ~0.8 because of kinetic effects in Rayleigh distillation and exchange reactions (as discussed in 4.2.2.4). As thermal maturity rises above 0.8%, the $\Delta^{13}CH_3D$ value increases and approaches thermodynamic equilibrium at maturity Easy%RoV > ~1.1 (Fig. 8b, d).

The predictions of our model fit the $\delta^{13}C$, δD, $\Delta^{12}CH_2D_2$ and $\Delta^{13}CH_3D$ data of natural thermogenic methanes generally well (Young et al., 2017; Gonzalez et al., 2019) (Fig. 8). $\Delta^{13}CH_3D$ and $\Delta^{12}CH_2D_2$ values of some of these methanes are higher than expected for their $\delta^{13}C$ values (Fig. 8c, d). This may reflect the possible migration of methane to reservoirs colder than its production temperature, which may cause isotope compositions to re-equilibrate to the lower storage temperature (this effect is not included in our model). Additionally, our model predictions fit well with the trend in isotopic composition of some methanes from Southwest Ontario and the Michigan Basin, which were previously interpreted to be mixtures of thermogenic and microbial gases (Giunta et al., 2019). We discuss this observation in section 4.4.

There are a few caveats in extrapolating the cracking-exchange model of n-octadecane pyrolysis to modeling of natural gas formation. We modeled a closed system where all generated methane is accumulated in the product, whereas natural gases often have semi-open reservoirs (Xia and Gao, 2019). Additionally, the thermal cracking of a pure compound such as n-octadecane and hydrogen exchange among hydrocarbons may not adequately represent the range of reactions taking place during the cracking and maturation of kerogens or crude oils (Tang et al., 2000). Despite these potential shortcomings, the trend of isotopic compositions of methane predicted by the model is consistent with data obtained for natural thermogenic methanes.

4.4. Implications for the interpretation of clumped isotope compositions of methane in natural gases

Giunta et al. (2019) examined gases in Southwest Ontario and the Michigan Basin from Cambrian to Devonian strata. The high C_1/C_{2+} ratio in many Antrim Shale gases (30 to 300) (Upper Devonian strata in Michigan Basin) suggests significant microbial contributions, from either microbial methanogenesis or secondary microbial degradation of hydrocarbons. In this previous study, Silurian gases have negative and varied $\Delta^{12}CH_2D_2$ compositions (-23 to 1‰), whereas the Ordovician and Cambrian gases appear to have clumped isotope compositions consistent with thermodynamic equilibrium. Giunta and colleagues proposed a two-end-member mixing model, including a thermogenic equilibrium end member and a microbial disequilibrium end member. Note that some variations in the 'wetness' of thermogenic end members are required by this model to fit data from different suites.

Based on our experimental results and cracking-exchange model, we suggest an alternative hypothesis for the Silurian gases that exhibit deficits in $\Delta^{12}CH_2D_2$ values. We suggest that they are early-oil- to early-gas-window thermogenic methanes that retain some part of the signature of

the combinatorial effect on their $\Delta^{12}CH_2D_2$ values during formation. This hypothesis is supported by the low thermal maturity of the *in situ* source and host rocks (Barker and Pollock, 1984; Sherwood Lollar et al., 1994), the low C_1/C_{2+} ratio of those gases, and the disequilibrium hydrogen isotope fractionation between methane and co-existing water. Consistent with the cracking-exchange model for natural methane formation in section 4.3, older gases from Cambrian and Ordovician strata in Southwest Ontario exhibit equilibrated $\Delta^{13}CH_3D$ and $\Delta^{12}CH_2D_2$ and equilibrated hydrogen isotope fractionations between methane and water. These equilibria may result from isotope exchange with water after a long enough period at their burial temperatures. $\delta^{13}C$, δD, $\Delta^{12}CH_2D_2$ and $\Delta^{13}CH_3D$ data of gases from Southwest Ontario and Michigan Basin (except for the Devonian Antrim Shale, where a microbial component seems clearly implicated (Martini et al., 1996)), can be explained by the cracking-exchange model for natural gases, especially considering a variation in $\delta^{13}C$ values of organic precursors (Fig. 8). $\Delta^{13}CH_3D$ and $\Delta^{12}CH_2D_2$ values higher than model prediction could result from cooling and re-equilibration after reaching the maximum burial temperature.

Gonzalez et al. (2019) measured an oil-associated thermogenic gas of early-oil-window maturity. Consistent with the cracking-exchange model for natural gases presented here, this oil-window gas has low $\delta^{13}C$ (−58.12±0.02‰), and non-equilibrated and depleted $\Delta^{12}CH_2D_2$ (0.8±0.8‰). This gas falls close to the trends predicted here in δD - $\delta^{13}C$ and $\Delta^{13}CH_3D$ - $\Delta^{12}CH_2D_2$ plots, but deviates from the predicted $\delta^{13}C$ - $\Delta^{12}CH_2D_2$ and $\delta^{13}C$ - $\Delta^{13}CH_3D$ relationship (Fig. 8). Although the model can qualitatively explain the disequilibrium in $\Delta^{12}CH_2D_2$, further quantitative discussion requires knowledge of geological burial history and precursors to methane in this gas.

Methane from the Beecher Island gas field shows a resolvable depletion (2.96‰) in $\Delta^{12}CH_2D_2$ relative to equilibrium at the apparent $\Delta^{13}CH_3D$ temperature of 142°C (Young et al., 2017). Although the disequilibrium in $\Delta^{12}CH_2D_2$ value resembles that of the oil-associated thermogenic gas in Gonzalez et al. (2019), the Beecher Island gas was attributed to a microbial origin as the $\delta^{13}C$ and δD of the methane fall in the microbial region on the Whiticar plot (Whiticar, 1999; Young et al., 2017; Milkov and Etiope, 2018). Future study may investigate whether the Beecher Island gas could be affected by mixing processes or by multiple thermogenic and microbial processes.

We also note that the depletion in $\Delta^{13}CH_3D$ and $\Delta^{12}CH_2D_2$ within early gas window (equivalent thermal maturity 0.8-1.2%Ro) will cause the Δ_{18} of methane to be depleted relative to equilibrium values. In our model, Δ_{18} is 1‰ lower than thermodynamic equilibrium at maturity Easy%RoV ~1, and Δ_{18} becomes indistinguishable from equilibrium at Easy%RoV > ~1.2. Therefore, the non-equilibrium Δ_{18} composition of unconventional oil-associated gases could be explained by kinetic effects in methane generation and hydrogen exchange and the combinatorial effects on $\Delta^{12}CH_2D_2$ (Douglas et al., 2017; Stolper et al., 2018; Xia and Gao, 2019).

4.5. Implications for the role of the combinatorial effect in abiogenesis and biogenesis of methane

Previous studies have argued that large depletions in $\Delta^{12}CH_2D_2$ of methane generated by the Sabatier reaction in the laboratory result from hydrogen quantum tunneling (Young et al., 2017; Young, 2019). However, the quantum tunneling model failed to explain the observed clumped

isotope effects and δD values simultaneously (Young et al., 2017; Cao et al., 2019). Alternatively, the depleted $\Delta^{12}CH_2D_2$ could be explained by the combinatorial effect of assembling hydrogen of different isotopic compositions (Cao et al., 2019). According to the reaction scheme of Fischer-Tropsch type reactions (Young et al., 2017), methane production from CO and H_2 starts with forming a CH species through hydrogen addition to an oxygen-bonded carbon and dehydroxylation of an OH group; next, three hydrogen atoms are added to the CH successively. Therefore, it is possible that the first hydrogen is affected by isotope effects different from those affecting the last three added hydrogens (and those three might differ from one another for more subtle reasons relating to the evolving structures of the intermediates). Any such combinatorial effects will cause deficits in $\Delta^{12}CH_2D_2$. Cao et al. (2019) proposed a marginally different mechanism for this experiment where the addition of the first two hydrogens is considered reversible, while the addition of the last two hydrogens is considered irreversible. If distinct isotope effects are expressed in reversible and irreversible steps in this mechanism, the combinatorial effects will also cause deficits in $\Delta^{12}CH_2D_2$.

A similar combinatorial effect is also expected in the experimental decomposition of tetrakis(trimethylsilyl) silane in Young et al., (2017). Methane is produced by CH_3 escaping from the silane structure followed by the addition of hydrogen. If the CH_3 and the capping hydrogen have distinct D/H, the combinatorial effect will cause a deficit in $\Delta^{12}CH_2D_2$. This deficit may have been erased by hydrogen exchange during heating at 300-600°C for tens of days, explaining why these higher temperature experiments produce methane that approaches equilibrium.

The combinatorial effect could also cause a deficit in $\Delta^{12}CH_2D_2$ of microbial methane if hydrogen atoms source from two or more isotopically different pools, e.g., from water, a reduced hydrogen pool, sulfur-bonded hydrogen, or carbon-bonded hydrogen (Valentine et al., 2004; Scheller et al., 2013; Greening et al., 2016; Young et al., 2017; Giunta et al., 2019; Cao et al., 2019). In fact, a combinatorial effect has been observed and studied in methane production by *Pseudomonas stutzeri* cultures, as discussed in 4.2.2.4 (Taenzer et al., 2020).

In conclusion, when four hydrogens in methane are sourced from isotopically different pools or fractionated by distinct isotope effects, there will be a combinatorial effect, irrespective of the conditions, mechanisms, and substrates of methanogenesis; the commonality of this mechanism provides a ready explanation for the similarities in clumped isotope systematics (particularly large depletion in $\Delta^{12}CH_2D_2$) in microbial, (putative) abiotic and thermogenic methane generated at early-oil to early-gas window maturities. An important implication of this conclusion is that $\Delta^{12}CH_2D_2$ alone is not a unique signature for abiotic or microbial methane.

4.6. Distinguishing thermogenic, microbial and abiotic methane by isotopic compositions

We compiled published $\delta^{13}C$, δD, $\Delta^{13}CH_3D$ and $\Delta^{12}CH_2D_2$ of natural methanes and examined whether data are organized into forensically diagnostic fields in plots of $\Delta^{13}CH_3D$ vs. $\Delta^{12}CH_2D_2$ and $\delta^{13}C$ - $\Delta^{12}CH_2D_2$ (Fig. 9a, b). We also plotted these natural methanes on the Whiticar plot with genetic fields from Milkov and Etiope (2018) (Fig. 9c).

When both $\Delta^{13}CH_3D$ and $\Delta^{12}CH_2D_2$ are in equilibrium at temperatures >100°C, and $\delta^{13}C$ and δD values are consistent with the widely recognized thermogenic range (Milkov and Etiope, 2018)

(Fig. 9c), it seems robust to identify such methane as thermogenic gas (Fig. 9a). However, we propose a second, disequilibrium thermogenic field based on our cracking-exchange model (Fig. 8) for natural gases (Fig. 9a, b). For this disequilibrium thermogenic field, we propose a wide range in $\Delta^{12}CH_2D_2$ values (starting with ~ -40‰ and approaching equilibrium values expected for 100 to 250°C). The $\delta^{13}C$ of the proposed field extends from ~ -65 to -45‰ and co-evolves with $\Delta^{12}CH_2D_2$ (Fig. 9b). We suggest a relatively broad range of $\Delta^{13}CH_3D$ values (~0 to 4‰) (Fig. 9a), which is consistent with the prediction by cracking-exchange model for natural thermogenic methane (Fig. 8b). Thermogenic gas in this field is interpreted to have been generated at early-oil to early-gas window maturities (est. %Ro ~ 0.6-1.2, Fig 8).

Microbial methane in a plot of $\Delta^{13}CH_3D$ - $\Delta^{12}CH_2D_2$ extends from the equilibrated composition at temperatures <100°C to negative values ($\Delta^{13}CH_3D$ ~ -1.2‰ and $\Delta^{12}CH_2D_2$ ~ -37‰, Fig. 9a). The wide distribution of microbial methane across this field likely reflects variations in substrate limitation and reversibility of microbial methanogenesis, and other equilibration processes, such as anaerobic oxidation of methane (Martini et al., 1996; Wang et al., 2015; Stolper et al., 2015; Gruen et al., 2018; Ash et al., 2019; Ono et al., 2021).

The compositional fields for microbial and disequilibrium thermogenic gases overlap between $\Delta^{13}CH_3D$ of ~ 0 to 3‰ and $\Delta^{12}CH_2D_2$ of -10 to -35‰, as well as between $\delta^{13}C$ of ~ -65 to -50‰ and $\delta^{13}D$ of ~ -350 to -250‰ (Fig. 9). These overlapping fields mean that subsets of thermogenic methane and microbial methane cannot be distinguished using bulk or clumped isotopes. In these cases, other information, such as gas chemistry and contextual geological data, may be the only useful discriminants. However, the subset of microbial methane having $\Delta^{13}CH_3D$ values < ~0‰ or > 4‰, or $\delta^{13}C$ less than ~ -70 ‰ appears to have no equivalents among methanes produced by catagenesis.

Methane of a putative abiotic origin is so far most distinct from other methane sources in the $\delta^{13}C$ – $\Delta^{12}CH_2D_2$ plot (Fig. 9b). The putative abiotic fields are characterized by relatively high $\delta^{13}C$, sometimes accompanied by a deficit in $\Delta^{12}CH_2D_2$ (e.g., Kidd Creek), or with $\Delta^{13}CH_3D$ or $\Delta^{12}CH_2D_2$-based temperatures of ~60-400°C (e.g., Chimaera, and hydrothermal methanes). Additionally, note that microbial processes could affect the pristine abiotic signature and drive clumped isotopes to equilibrium at environmental temperatures (e.g., fresh Kidd Creek versus old Kidd Creek in Fig. 9, Ash et al., 2019).

Overall, $\Delta^{13}CH_3D$ and $\Delta^{12}CH_2D_2$ compositions provide additional information to sourcing methane in supplement to $\delta^{13}C$ and δD. However, initial suggestions that these clumped isotope proxies commonly provide unique signatures of biogenesis or abiogenesis appear to be untrue. Early catagenesis is a widespread process that yields abundant methane, potentially having isotopic signatures resembling some microbial and putative abiotic gases. In any case, we expect the genetic fields in Fig. 9a and Fig. 9b to expand as future researches characterize clumped isotope compositions of more natural methanes.

5. SUMMARY AND CONCLUSIONS

We performed controlled pyrolysis experiments on n-octadecane ($C_{18}H_{38}$) at 400°C. We found that $\Delta^{13}CH_3D$ values of generated methane appear to be consistent with thermodynamic

equilibrium at the experimental temperature, whereas $\Delta^{12}CH_2D_2$ values are 30 to 40‰ depleted compared with equilibrium. Values of $\Delta^{12}CH_2D_2$ increase with advancing pyrolysis progress. We quantitatively demonstrated that the large deficit in $\Delta^{12}CH_2D_2$ can result from the combinatorial effect in assembling hydrogen from isotopically-different pools into a methane molecule. The increase of $\Delta^{12}CH_2D_2$ with experimental time can be explained by partial equilibration of methane through hydrogen exchange with co-existing hydrocarbons.

We propose a cracking-exchange model for isotope signatures of thermogenic methane, including singly and doubly-substituted species, during generation, maturation and equilibration of natural gas. This model can explain the isotopic compositions of thermogenic methane that have been published to date. However, there is at present an underappreciation of the potential for such signatures among thermogenic natural gases, and more natural samples, particularly methane generated at early-gas window maturities, should be examined and compared with the model.

Our model for thermogenic methane also reveals that early-oil to early-gas window thermogenic methane has isotopic compositions ($\delta^{13}C$, δD, $\Delta^{13}CH_3D$, and $\Delta^{12}CH_2D_2$) similar to microbial methane. Although this similarity leads to difficulty in distinguishing early thermogenic methane from microbial methane using clumped isotopes, one could still recognize those early thermogenic gases by $\delta^{13}C$ of C_1-C_5 gas compounds, which generally plot in straight lines on the 'Chung plot' (Chung et al., 1988), or by the presence of higher alkanes, like C_{4+} , which are not recognized as possibly produced by microbial metabolisms (Milkov and Etiope, 2018).

More generally, the combination of our findings with those from prior studies suggests a common theme to the isotopic structures of methanes formed by important natural processes: If the methane generation pathway uses methyl as a precursor and is irreversible, $\Delta^{13}CH_3D$ of methane will partially inherit the initial $\Delta^{13}CH_2D$ of the methyl group, while $\Delta^{12}CH_2D_2$ will be controlled by the difference in δD between the methyl group and the capping hydrogen; if δD of the methyl group and the capping hydrogen are very close, $\Delta^{12}CH_2D_2$ will inherit the initial $\Delta^{12}CHD_2$ value of the methyl group, whereas when these two pools differ in δD, large $\Delta^{12}CH_2D_2$ deficits will result. This model for the interpretation of methane clumped isotope compositions suggests that we should prioritize future studies of the clumped isotope compositions of methyl groups in potential methane precursors (Lloyd et al., 2020).

Last but not least, hydrogen exchange reactions have been proposed or predicted to cause non-equilibrium signatures in clumped isotope compositions of methane in this study, Xia and Gao (2019), Labidi et al. (2020) and Giunta et al. (2021). These discussions would fundamentally benefit from systematic experimental investigation on the kinetics of hydrogen exchange among isotopologues of methane, and between methane and other hydrogen-bearing substrates (e.g., water and hydrocarbons).

ACKNOWLEDGEMENT

This work was supported by Caltech, ExxonMobil Upstream Integrated Solutions (formerly Upstream Research Company), the Caltech Joint Industry Partnership for Petroleum Geochemistry, Thermo Fischer Scientific, and the Department of Energy BES program. We

thank Nami Kitchen, Nithya Thiagarajan, Yanhua Shuai, Newton Nguyen, and David Wang for helpful discussions. We thank Xinyu Xia and two anonymous reviewers for helpful comments.

FIGURE CAPTIONS

Fig. 1. Time evolution of (a) yield and (b) dryness of gas products in pyrolysis of n-octadecane. The yield is expressed in carbon-mole-ratio, which is the molar ratio of carbon in the gas component (i.e., methane, ethane, or propane) divided by that in the starting n-octadecane. Methane yield curve modeled by the cracking and cracking-exchange model (yellow dashed line) fits the experimental data with R^2 of 0.73.

Fig. 2. Time evolution of compound-specific (a) carbon and (b) hydrogen isotope compositions of gas products in pyrolysis of n-octadecane. Error bars are smaller than the symbols.

Fig. 3. (a) carbon and hydrogen isotope and (b) clumped-isotope compositions of methane generated in pyrolysis of n-octadecane. The data points for pyrolysis products are color-coded with Easy%RoV (Burnham, 2019). In (a), the error bars of pyrolysis products are smaller than the marker. Both $\delta^{13}C$ and δD increase with maturation. In (b), the solid line shows the thermodynamic equilibrium $\Delta^{13}CH_3D$ and $\Delta^{12}CH_2D_2$ values from 2000 to 0°C (Eldridge et al., 2019a). The equilibrated value at labeled temperatures (°C) are marked as black dots. The $\Delta^{13}CH_3D$ values of methane products appear to be within 2 standard errors (2 SE) of the expected equilibrium composition, whereas the $\Delta^{12}CH_2D_2$ values are much more depleted than equilibrium and do not correspond to any possible temperature. Moreover, the $\Delta^{12}CH_2D_2$ values are progressively approaching the equilibrium value with maturation.

Fig. 4. Chung plot for product gas components (methane, ethane, propane, and n-butane) in pyrolysis of n-octadecane (Chung et al., 1988). Components at each experimental time have a negative linear correlation between $\delta^{13}C$ and 1/N (linear regression data in Table 3), where N is the number of carbon atoms in each of the product molecules. The intercepts increase as pyrolysis proceeds (except for one outlier), whereas the slopes do not change systematically throughout the experimental period (Table 3).

Fig. 5. Cartoon representation of methane generation in pyrolysis of n-octadecane. Methane generation starts with producing a methyl radical by breaking a carbon-carbon bond through homolytic cleavage or β scission. Then the methyl radical attacks co-existing hydrogen bearing compounds (i.e. hydrocarbons including precursor n-octadecane) and abstracts the capping hydrogen. The three hydrogen atoms from the methyl precursor in each methane molecule constitute a pool with higher deuterium concentration, whereas the capping hydrogen makes up a second pool with lower deuterium concentration. Nevertheless, the four hydrogen atoms are symmetrically equivalent in a product methane molecule. This symmetric equivalence leads one to predict a stochastic abundance of $^{12}CH_2D_2$ that is much higher than the true probability of randomly forming $^{12}CH_2D_2$ – this phenomenon is the 'combinatorial effect'. When four hydrogens in methane are sourced from isotopically different pools or fractionated by distinct isotope effects, there will be a combinatorial effect, causing a deficit in $\Delta^{12}CH_2D_2$ but not affecting $\Delta^{13}CH_3D$.

Fig. 6. The optimal cracking model results (blue line) fitted to pyrolysis experiment results (yellow circles) (Table 5). The cracking model fits the trend in $\delta^{13}C$ with an R-square of 0.71 and fits the $\Delta^{13}CH_3D$ values to within 2 standard errors. However, this model was not capable of

finding a solution that fit the trends for δD and $\Delta^{12}CH_2D_2$ to within small multiples of their respective errors (see also Fig. A1). On the contrary, the model predicts a decreasing trend in $\Delta^{12}CH_2D_2$ with increasing reaction progress and a slower rate of increase in δD with time. Error bars are 1 standard experimental errors.

Fig. 7. The optimal cracking-exchange model results (blue line) fitted to pyrolysis experiment results (yellow circles) (Table 5). The cracking-exchange model fits $\delta^{13}C$, δD and $\Delta^{12}CH_2D_2$ with an R-square of 0.71, 0.87, and 0.58, and fits the $\Delta^{13}CH_3D$ values to within 2-3 standard errors at all reaction progress values. All major features of the data can be explained, especially the enrichment in $\Delta^{12}CH_2D_2$ and δD as pyrolysis proceeds. Error bars are 1 standard experimental errors.

Fig. 8. Modeling the generation, maturation and equilibration of natural thermogenic methane (Table 6, Appendix A2) with $\delta^{13}C$ of the organic precursor as -30, -25, and -20‰. This model predicts $\delta^{13}C$ and δD (a) increase with thermal maturity (%Ro) until δD reaches equilibrium with co-existing hydrogen-bearing compounds at ~1.5%Ro. $\Delta^{13}CH_3D$ and $\Delta^{12}CH_2D_2$ are insensitive to $\delta^{13}C$ of the organic precursor (b). $\Delta^{12}CH_2D_2$ (b, c) increases from ~ -60‰ at ~ 0.6%Ro, to ~0‰ at 1.0%Ro, and reaches equilibrium at burial temperature at maturity > ~1.1%Ro. $\Delta^{13}CH_3D$ (b, d) first decreases at maturity < ~ 0.8%Ro, then increases at 0.8-1.0%Ro and approach equilibrium at ~1.2%Ro. For mature gases with %Ro >1.5, clumped isotope compositions are fully equilibrated. The predictions are consistent with the trend of data for natural thermogenic methanes and suggest an alternative thermogenic origin for the deficits in $\Delta^{12}CH_2D_2$ of some natural gases. Yellow and brown crosses indicate equivalent thermal maturity of 0.6, 0.8, 1.0, 1.2 and 1.5%Ro (color-coated with Easy%RoV). The black cross in (b) indicates 1 SE of analyses. Data from this study, Young et al. (2017), Giunta et al. (2019), Gonzalez et al. (2019).

Fig. 9. Diagrams of (a) $\Delta^{13}CH_3D$ - $\Delta^{12}CH_2D_2$, (b) $\delta^{13}C$ - $\Delta^{12}CH_2D_2$ and (c) $\delta^{13}C$ - δD with forensically diagnostic fields. We propose a disequilibrium thermogenic field based on a cracking-exchange model for natural thermogenic methane. Clumped isotope data from Young et al. (2017), Giunta et al. (2019), Ash et al. (2019), Gonzalez et al. (2019), Young (2019), Thiagarajan et al. (2020a), Labidi et al. (2020), and Giunta et al. (2021). Original data of boreal lake were not provided and thus cannot be plotted on (b). Genetic fields on (c) from Milkov and Etiope (2018) and Miller et al. (2018) (see also Fiebig et al. (2019b) and Reeves and Fiebig (2020) for $\delta^{13}C$ - δD values of volcanic-hydrothermal methane).

Fig. A1. Sensitivity tests on the primary deuterium KIE of B-D ($^{D}KIE_{PRI}$), and secondary deuterium KIE of A-$^{12}CH_2D$ ($^{D}KIE_{SEC}$) on the cracking model. The change of δD (a) and $\Delta^{12}CH_2D_2$ (b) when varying $^{D}KIE_{PRI}$ from 0.30 to 0.40 ($^{D}KIE_{SEC}$ = 0.92) and the change of δD (c) and $\Delta^{12}CH_2D_2$ (d) when varying $^{D}KIE_{SEC}$ from 0.88 to 0.96 ($^{D}KIE_{PRI}$ = 0.35) demonstrate that the absolute values of $^{D}KIE_{PRI}$ and $^{D}KIE_{SEC}$ controls δD, and that the relative difference in $^{D}KIE_{PRI}$ and $^{D}KIE_{SEC}$ controls $\Delta^{12}CH_2D_2$. $\delta^{13}C$ and $\Delta^{13}CH_3D$ are not sensitive to $^{D}KIE_{PRI}$ and $^{D}KIE_{SEC}$. Values of other parameters in Table 5.

REFERENCES

Ash J. L., Egger M., Treude T., Kohl I., Cragg B., Parkes R. J., Slomp C. P., Sherwood Lollar B. and Young E. D. (2019) Exchange catalysis during anaerobic methanotrophy revealed by 12CH2D2 and 13CH3D in methane. *Geochemical Perspectives Letters*, 26–30.

Bajnai D., Guo W., Spötl C., Coplen T. B., Methner K., Löffler N., Krsnik E., Gischler E., Hansen M., Henkel D., Price G. D., Raddatz J., Scholz D. and Fiebig J. (2020) Dual clumped isotope thermometry resolves kinetic biases in carbonate formation temperatures. *Nature Communications* **11**.

Barker J. F. and Pollock S. J. (1984) The geochemistry and origin of natural gases in Southern Ontario. *Bull. Can. Pet. Geol.* **32**, 313–326.

Bigeleisen J. and Wolfsberg M. (1957) Theoretical and Experimental Aspects of Isotope Effects in Chemical Kinetics. In *Advances in Chemical Physics* (eds. I. Prigogine and P. Debye). John Wiley & Sons, Inc., Hoboken, NJ, USA. pp. 15–76.

Billault I., Guiet S., Mabon F. and Robins R. (2001) Natural Deuterium Distribution in Long-Chain Fatty Acids Is Nonstatistical: A Site-Specific Study by Quantitative2H NMR Spectroscopy. *ChemBioChem* **2**, 425–431.

Burnham A. K. (2019) Kinetic models of vitrinite, kerogen, and bitumen reflectance. *Organic Geochemistry* **131**, 50–59.

Canadell E. and Olivella S. (1984) Theoretical analysis of kinetic isotope effects. Deuterium isotope effects in the reaction of methyl with methane. *The Journal of Physical Chemistry* **88**, 3545–3549.

Cao X., Bao H. and Peng Y. (2019) A kinetic model for isotopologue signatures of methane generated by biotic and abiotic CO2 methanation. *Geochimica et Cosmochimica Acta* **249**, 59–75.

Chung H. M., Gormly J. R. and Squires R. M. (1988) Origin of gaseous hydrocarbons in subsurface environments: Theoretical considerations of carbon isotope distribution. *Chemical Geology* **71**, 97–104.

Chung H. M., Rooney M. A., Toon M. B. and Claypool G. E. (1992) Carbon Isotope Composition of Marine Crude Oils. *AAPG Bulletin* **76**.

Clog M., Lawson M., Peterson B., Ferreira A. A., Santos Neto E. V. and Eiler J. M. (2018) A reconnaissance study of 13C–13C clumping in ethane from natural gas. *Geochimica et Cosmochimica Acta* **223**, 229–244.

Douglas P. M. J., Stolper D. A., Eiler J. M., Sessions A. L., Lawson M., Shuai Y., Bishop A., Podlaha O. G., Ferreira A. A., Santos Neto E. V., Niemann M., Steen A. S., Huang L., Chimiak L., Valentine D. L., Fiebig J., Luhmann A. J., Seyfried W. E., Etiope G., Schoell

M., Inskeep W. P., Moran J. J. and Kitchen N. (2017) Methane clumped isotopes: Progress and potential for a new isotopic tracer. *Organic Geochemistry* **113**, 262–282.

Douglas P. M. J., Stolper D. A., Smith D. A., Walter Anthony K. M., Paull C. K., Dallimore S., Wik M., Crill P. M., Winterdahl M., Eiler J. M. and Sessions A. L. (2016) Diverse origins of Arctic and Subarctic methane point source emissions identified with multiply-substituted isotopologues. *Geochimica et Cosmochimica Acta* **188**, 163–188.

Eldridge D. L., Korol R., Lloyd M. K., Turner A. C., Webb M. A., Miller T. F. and Stolper D. A. (2019a) Comparison of Experimental vs Theoretical Abundances of $^{13}CH_3D$ and $^{12}CH_2D_2$ for Isotopically Equilibrated Systems from 1 to 500 °C. *ACS Earth and Space Chemistry* **3**, 2747–2764.

Eldridge D. L., Lloyd M. K. and Stolper D. A. (2019b) Methane Clumped Isotope Compositions From Ethane Pyrolysis Experiments. *Goldschmidt Abstracts* **2019**.

Etiope G. and Sherwood Lollar B. (2013) ABIOTIC METHANE ON EARTH: ABIOTIC METHANE ON EARTH. *Reviews of Geophysics* **51**, 276–299.

Fiebig J., Bajnai D., Löffler N., Methner K., Krsnik E., Mulch A. and Hofmann S. (2019a) Combined high-precision Δ48 and Δ47 analysis of carbonates. *Chemical Geology* **522**, 186–191.

Fiebig J., Stefánsson A., Ricci A., Tassi F., Viveiros F., Silva S., Lopez T. M., Schreiber C., Hofmann S. and Mountain B. W. (2019b) Abiogenesis not required to explain the origin of volcanic-hydrothermal hydrocarbons. *Geochemical Perspectives Letters*, 23–27.

Giunta T., Labidi J., Kohl I. E., Ruffine L., Donval J. P., Géli L., Çağatay M. N., Lu H. and Young E. D. (2021) Evidence for methane isotopic bond re-ordering in gas reservoirs sourcing cold seeps from the Sea of Marmara. *Earth and Planetary Science Letters* **553**, 116619.

Giunta T., Young E. D., Warr O., Kohl I., Ash J. L., Martini A., Mundle S. O. C., Rumble D., Pérez-Rodríguez I., Wasley M., LaRowe D. E., Gilbert A. and Sherwood Lollar B. (2019) Methane sources and sinks in continental sedimentary systems: New insights from paired clumped isotopologues 13CH3D and 12CH2D2. *Geochimica et Cosmochimica Acta* **245**, 327–351.

Gonzalez Y., Nelson D. D., Shorter J. H., McManus J. B., Dyroff C., Formolo M. J., Wang D. T., Western C. M. and Ono S. (2019) Precise measurements of 12CH2D2 by tunable infrared laser direct absorption spectroscopy. *Analytical Chemistry*.

Gray P., Herod A. A. and Jones A. (1971) Kinetic data for hydrogen and deuterium atom abstraction by methyl and trifluoromethyl radicals in the gaseous phase. *Chemical Reviews* **71**, 247–294.

Greening C., Ahmed F. H., Mohamed A. E., Lee B. M., Pandey G., Warden A. C., Scott C., Oakeshott J. G., Taylor M. C. and Jackson C. J. (2016) Physiology, Biochemistry, and

Applications of F_{420} - and F_o -Dependent Redox Reactions. *Microbiology and Molecular Biology Reviews* **80**, 451–493.

Gruen D. S., Wang D. T., Könneke M., Topçuoğlu B. D., Stewart L. C., Goldhammer T., Holden J. F., Hinrichs K.-U. and Ono S. (2018) Experimental investigation on the controls of clumped isotopologue and hydrogen isotope ratios in microbial methane. *Geochimica et Cosmochimica Acta* **237**, 339–356.

Helgeson H. C., Richard L., McKenzie W. F., Norton D. L. and Schmitt A. (2009) A chemical and thermodynamic model of oil generation in hydrocarbon source rocks. *Geochimica et Cosmochimica Acta* **73**, 594–695.

Jackśon K. J., Burnham A. K., Braun R. L. and Knauss K. G. (1995) Temperature and pressure dependence of n-hexadecane cracking. *Organic Geochemistry* **23**, 941–953.

Jackson W. M., McNesby J. R. and Darwent B. deB. (1962) Reaction of Methyl- d_3 Radicals with Isobutane, Isobutane-2- *d,* and Propane. *The Journal of Chemical Physics* **37**, 1610–1615.

Jeffrey A. W. A. (1981) Thermal and clay catalysed cracking in the formation of natural gas. Ph.D. dissertation, Texas A&M University.

Jitariu L. C., Jones L. D., Robertson S. H., Pilling M. J. and Hillier I. H. (2003) Thermal Rate Coefficients via Variational Transition State Theory for the Unimolecular Decomposition/Isomerization of 1-Pentyl Radical: Ab Initio and Direct Dynamics Calculations. *The Journal of Physical Chemistry A* **107**, 8607–8617.

Johnston H. S. and Rapp D. (1961) Large Tunnelling Corrections in Chemical Reaction Rates. [1] II. *Journal of the American Chemical Society* **83**, 1–9.

Koepp M. (1978) D/H isotope exchange reaction between petroleum and water: A contributory determinant for D/H-isotope ratios in crude oils? *Short Papers of the Fourth International Conference, Geochronology, Cosmochronology, Isotope Geology 1978* **USGS Open-File Report 78-701 (ed. R. E. Zartman)**, 2.

Labidi J., Young E. D., Giunta T., Kohl I. E., Seewald J., Tang H., Lilley M. D. and Früh-Green G. L. (2020) Methane thermometry in deep-sea hydrothermal systems: Evidence for re-ordering of doubly-substituted isotopologues during fluid cooling. *Geochimica et Cosmochimica Acta* **288**, 248–261.

Lloyd M. K., Eldridge D. L. and Stolper D. A. (2020) Clumped 13CH2D and 12CHD2 compositions of methyl groups from wood and synthetic monomers: methods, experimental and theoretical calibrations, and initial results. *Geochimica et Cosmochimica Acta*.

Lu D. H., Maurice D. and Truhlar D. G. (1990) What is the effect of variational optimization of the transition state on .alpha.-deuterium secondary kinetic isotope effects? A prototype:

CD3H + H .dblarw. CD3 + H2. *Journal of the American Chemical Society* **112**, 6206–6214.

Mango F. D., Jarvie D. and Herriman E. (2009) Natural gas at thermodynamic equilibrium Implications for the origin of natural gas. *Geochemical Transactions* **10**.

Martin P. E. (2020) Detection and Analysis of Martian Low-Temperature Geochemistry. Ph.D. dissertation, California Institute of Technology. Available at: https://resolver.caltech.edu/CaltechTHESIS:12112019-142555725.

Martini A. M., Budai J. M., Walter L. M. and Schoell M. (1996) Microbial generation of economic accumulations of methane within a shallow organic-rich shale. *Nature* **383**, 155–158.

Milkov A. V. and Etiope G. (2018) Revised genetic diagrams for natural gases based on a global dataset of >20,000 samples. *Organic Geochemistry* **125**, 109–120.

Miller H. M., Chaudhry N., Conrad M. E., Bill M., Kopf S. H. and Templeton A. S. (2018) Large carbon isotope variability during methanogenesis under alkaline conditions. *Geochimica et Cosmochimica Acta* **237**, 18–31.

Neubauer C., Crémière A., Wang X. T., Thiagarajan N., Sessions A. L., Adkins J. F., Dalleska N. F., Turchyn A. V., Clegg J. A., Moradian A., Sweredoski M. J., Garbis S. D. and Eiler J. M. (2020) Stable Isotope Analysis of Intact Oxyanions Using Electrospray Quadrupole-Orbitrap Mass Spectrometry. *Analytical Chemistry*. Available at: https://pubs.acs.org/doi/abs/10.1021/acs.analchem.9b04486 [Accessed February 15, 2020].

Ni Y., Ma Q., Ellis G. S., Dai J., Katz B., Zhang S. and Tang Y. (2011) Fundamental studies on kinetic isotope effect (KIE) of hydrogen isotope fractionation in natural gas systems. *Geochimica et Cosmochimica Acta* **75**, 2696–2707.

Ono S., Rhim J. H., Gruen D. S., Taubner H., Kölling M. and Wegener G. (2021) Clumped isotopologue fractionation by microbial cultures performing the anaerobic oxidation of methane. *Geochimica et Cosmochimica Acta* **293**, 70–85.

Ono S., Wang D. T., Gruen D. S., Sherwood Lollar B., Zahniser M. S., McManus B. J. and Nelson D. D. (2014) Measurement of a Doubly Substituted Methane Isotopologue, $^{13}CH_3D$, by Tunable Infrared Laser Direct Absorption Spectroscopy. *Analytical Chemistry* **86**, 6487–6494.

Peters K. E., Walters C. C. and Moldowan J. M. (2004) *The Biomarker Guide*. 2nd ed., Cambridge University Press.

Peterson B. K., Formolo M. J. and Lawson M. (2018) Molecular and detailed isotopic structures of petroleum: Kinetic Monte Carlo analysis of alkane cracking. *Geochimica et Cosmochimica Acta* **243**, 169–185.

Piasecki A., Sessions A., Lawson M., Ferreira A. A., Neto E. V. S. and Eiler J. M. (2016a) Analysis of the site-specific carbon isotope composition of propane by gas source isotope ratio mass spectrometer. *Geochimica et Cosmochimica Acta* **188**, 58–72.

Piasecki A., Sessions A., Peterson B. and Eiler J. (2016b) Prediction of equilibrium distributions of isotopologues for methane, ethane and propane using density functional theory. *Geochimica et Cosmochimica Acta* **190**, 1–12.

Popa M. E., Paul D., Janssen C. and Röckmann T. (2019) H_2 clumped isotope measurements at natural isotopic abundances. *Rapid Communications in Mass Spectrometry* **33**, 239–251.

Reeves E. P. and Fiebig J. (2020) Abiotic Synthesis of Methane and Organic Compounds in Earth's Lithosphere. *Elements* **16**, 25–31.

Reeves E. P., Seewald J. S. and Sylva S. P. (2012) Hydrogen isotope exchange between n-alkanes and water under hydrothermal conditions. *Geochimica et Cosmochimica Acta* **77**, 582–599.

Röckmann T., Popa M. E., Krol M. C. and Hofmann M. E. G. (2016) Statistical clumped isotope signatures. *Scientific Reports* **6**.

Rooney M. A., Claypool G. E. and Moses Chung H. (1995) Modeling thermogenic gas generation using carbon isotope ratios of natural gas hydrocarbons. *Chemical Geology* **126**, 219–232.

Sackett W. M. (1978) Carbon and hydrogen isotope effects during the thermocatalytic production of hydrocarbons in laboratory simulation experiments. *Geochimica et Cosmochimica Acta* **42**, 571–580.

Salomon M. (1964) ISOTOPE EFFECTS IN METHYL RADICAL ABSTRACTION REACTIONS. *Canadian Journal of Chemistry* **42**, 610–613.

Scheller S., Goenrich M., Thauer R. K. and Jaun B. (2013) Methyl-Coenzyme M Reductase from Methanogenic Archaea: Isotope Effects on the Formation and Anaerobic Oxidation of Methane. *Journal of the American Chemical Society* **135**, 14975–14984.

Schimmelmann A., Sessions A. L. and Mastalerz M. (2006) HYDROGEN ISOTOPIC (D/H) COMPOSITION OF ORGANIC MATTER DURING DIAGENESIS AND THERMAL MATURATION. *Annual Review of Earth and Planetary Sciences* **34**, 501–533.

Schoell M. (1984) Recent advances in petroleum isotope geochemistry. *Organic Geochemistry* **6**, 645–663.

Seewald J. S. (1994) Evidence for metastable equilibrium between hydrocarbons under hydrothermal conditions. *Nature* **370**, 285–287.

Sessions A. L. (2016) Factors controlling the deuterium contents of sedimentary hydrocarbons. *Organic Geochemistry* **96**, 43–64.

Sessions A. L., Sylva S. P., Summons R. E. and Hayes J. M. (2004) Isotopic exchange of carbon-bound hydrogen over geologic timescales 1 1Associate editor: J. Horita. *Geochimica et Cosmochimica Acta* **68**, 1545–1559.

Sherwood Lollar B., Weise S. M., Frape S. K. and Barker J. F. (1994) Isotopic constraints on the migration of hydrocarbon and helium gases of southwestern Ontario. *Bull. Can. Pet. Geol.* **42**, 283–295.

Shuai Y., Douglas P. M. J., Zhang S., Stolper D. A., Ellis G. S., Lawson M., Lewan M. D., Formolo M., Mi J., He K., Hu G. and Eiler J. M. (2018) Equilibrium and non-equilibrium controls on the abundances of clumped isotopologues of methane during thermogenic formation in laboratory experiments: Implications for the chemistry of pyrolysis and the origins of natural gases. *Geochimica et Cosmochimica Acta* **223**, 159–174.

Singleton D. A. and Thomas A. A. (1995) High-Precision Simultaneous Determination of Multiple Small Kinetic Isotope Effects at Natural Abundance. *Journal of the American Chemical Society* **117**, 9357–9358.

Stolper D. A., Lawson M., Davis C. L., Ferreira A. A., Neto E. V. S., Ellis G. S., Lewan M. D., Martini A. M., Tang Y., Schoell M., Sessions A. L. and Eiler J. M. (2014) Formation temperatures of thermogenic and biogenic methane. *Science* **344**, 1500–1503.

Stolper D. A., Lawson M., Formolo M. J., Davis C. L., Douglas P. M. J. and Eiler J. M. (2018) The utility of methane clumped isotopes to constrain the origins of methane in natural gas accumulations. *Geological Society, London, Special Publications* **468**, 23–52.

Stolper D. A., Martini A. M., Clog M., Douglas P. M., Shusta S. S., Valentine D. L., Sessions A. L. and Eiler J. M. (2015) Distinguishing and understanding thermogenic and biogenic sources of methane using multiply substituted isotopologues. *Geochimica et Cosmochimica Acta* **161**, 219–247.

Stolper D.A., Sessions A. L., Ferreira A. A., Santos Neto E. V., Schimmelmann A., Shusta S. S., Valentine D. L. and Eiler J. M. (2014) Combined 13C–D and D–D clumping in methane: Methods and preliminary results. *Geochimica et Cosmochimica Acta* **126**, 169–191.

Sweeney J. J. and Burnham A. K. (1990) Evaluation of a simple model of vitrinite reflectance based on chemical kinetics. *AAPG Bulletin* **74**, 1559–1570.

Taenzer L., Labidi J., Masterson A. L., Feng X., Rumble D., Young E. D. and Leavitt W. D. (2020) Low Δ 12 CH 2 D 2 values in microbialgenic methane result from combinatorial isotope effects. *Geochimica et Cosmochimica Acta* **285**, 225–236.

Tang Y., Huang Y., Ellis G. S., Wang Y., Kralert P. G., Gillaizeau B., Ma Q. and Hwang R. (2005) A kinetic model for thermally induced hydrogen and carbon isotope fractionation of individual n-alkanes in crude oil. *Geochimica et Cosmochimica Acta* **69**, 4505–4520.

Tang Y., Perry J. K., Jenden P. D. and Schoell M. (2000) Mathematical modeling of stable carbon isotope ratios in natural gases. *Geochimica et Cosmochimica Acta* **64**, 2673–2687.

Thiagarajan N., Kitchen N., Xie H., Ponton C., Lawson M., Formolo M. and Eiler J. (2020a) Identifying thermogenic and microbial methane in deep water Gulf of Mexico Reservoirs. *Geochimica et Cosmochimica Acta* **275**, 188–208.

Thiagarajan N., Xie H., Ponton C., Kitchen N., Peterson B., Lawson M., Formolo M., Xiao Y. and Eiler J. (2020b) Isotopic evidence for quasi-equilibrium chemistry in thermally mature natural gases. *Proceedings of the National Academy of Sciences* **117**, 3989–3995.

Tissot B. P. and Welte D. H. (1984) *Petroleum formation and occurrence*. 2nd, rev.enl. ed ed., Springer-Verlag, Berlin ; New York.

Ueno Y., Katsuta T., Ishimaru T. and Yoshida N. (2019) A new method for measuring 34S-18O clumping of sulfate. *Goldschmidt Abstracts* **2019**.

Ungerer P., Behar F., Villalba M., Heum O. R. and Audibert A. (1988) Kinetic modelling of oil cracking. *Organic Geochemistry* **13**, 857–868.

Valentine D. L. (2011) Emerging Topics in Marine Methane Biogeochemistry. *Annual Review of Marine Science* **3**, 147–171.

Valentine D. L., Chidthaisong A., Rice A., Reeburgh W. S. and Tyler S. C. (2004) Carbon and hydrogen isotope fractionation by moderately thermophilic methanogens 1 1Associate editor: N. E. Ostrom. *Geochimica et Cosmochimica Acta* **68**, 1571–1590.

Wang D. T., Gruen D. S., Lollar B. S., Hinrichs K.-U., Stewart L. C., Holden J. F., Hristov A. N., Pohlman J. W., Morrill P. L., Konneke M., Delwiche K. B., Reeves E. P., Sutcliffe C. N., Ritter D. J., Seewald J. S., McIntosh J. C., Hemond H. F., Kubo M. D., Cardace D., Hoehler T. M. and Ono S. (2015) Nonequilibrium clumped isotope signals in microbial methane. *Science* **348**, 428–431.

Wang D. T., Reeves E. P., McDermott J. M., Seewald J. S. and Ono S. (2018) Clumped isotopologue constraints on the origin of methane at seafloor hot springs. *Geochimica et Cosmochimica Acta* **223**, 141–158.

Wang D. T., Welander P. V. and Ono S. (2016) Fractionation of the methane isotopologues 13 CH 4 , 12 CH 3 D, and 13 CH 3 D during aerobic oxidation of methane by Methylococcus capsulatus (Bath). *Geochimica et Cosmochimica Acta* **192**, 186–202.

Wang Y., Sessions A. L., Nielsen R. J. and Goddard W. A. (2009) Equilibrium 2H/1H fractionations in organic molecules. II: Linear alkanes, alkenes, ketones, carboxylic acids, esters, alcohols and ethers. *Geochimica et Cosmochimica Acta* **73**, 7076–7086.

Wang Y., Zhao Y., Liang C., Chen Y., Zhang Q. and Li X. (2017) Molecular-level modeling investigation of n-decane pyrolysis at high temperature. *Journal of Analytical and Applied Pyrolysis* **128**, 412–422.

Wei L., Gao Z., Mastalerz M., Schimmelmann A., Gao L., Wang X., Liu X., Wang Y. and Qiu Z. (2019) Influence of water hydrogen on the hydrogen stable isotope ratio of methane at low versus high temperatures of methanogenesis. *Organic Geochemistry* **128**, 137–147.

Whiticar M. J. (1999) Carbon and hydrogen isotope systematics of bacterial formation and oxidation of methane. *Chemical Geology* **161**, 291–314.

Xia X. and Gao Y. (2019) Kinetic clumped isotope fractionation during the thermal generation and hydrogen exchange of methane. *Geochimica et Cosmochimica Acta* **248**, 252–273.

Xiao Y. (2001) Modeling the Kinetics and Mechanisms of Petroleum and Natural Gas Generation: A First Principles Approach. *Reviews in Mineralogy and Geochemistry* **42**, 383–436.

Xie H., Dong G., Thiagarajan N., Shuai Y., Mangenot X., Formolo M. J., Lawson M. and Eiler J. M. (2019) Methane Clumped Isotopologues With High-resolution Gas Source Isotope Ratio Mass Spectrometry. In *AGU Fall Meeting Abstracts* pp. V14B-05.

Xie H., Ponton C., Formolo M. J., Lawson M., Ellis G. S., Lewan M. D., Ferreira A. A., Morais E. T., Spigolon A. L. D., Sessions A. L. and Eiler J. M. (2020) Position-specific distribution of hydrogen isotopes in natural propane: Effects of thermal cracking, equilibration and biodegradation. *Geochimica et Cosmochimica Acta* **290**, 235–256.

Xie H., Ponton C., Formolo M. J., Lawson M., Peterson B. K., Lloyd M. K., Sessions A. L. and Eiler J. M. (2018) Position-specific hydrogen isotope equilibrium in propane. *Geochimica et Cosmochimica Acta* **238**, 193–207.

Yeung L. Y. (2016) Combinatorial effects on clumped isotopes and their significance in biogeochemistry. *Geochimica et Cosmochimica Acta* **172**, 22–38.

Yi J., Jun L., Jing-Bo W., Jian-Li W., Quan Z., Yao-Qiang C., Xiang-Yuan L., 四川大学化学学院, 成都 610065;,College of Chemistry, Sichuan University, Chengdu 610065, P. R. China;, and 四川大学化工学院, 成都 610065,College of Chemical Engineering, Sichuan University, Chengdu 610065, P. R. China (2011) Experiment and Kinetics Simulation on the Pyrolysis of n-Decane. *Acta Physico-Chimica Sinica* **27**, 1061–1067.

Yoshinaga M. Y., Holler T., Goldhammer T., Wegener G., Pohlman J. W., Brunner B., Kuypers M. M. M., Hinrichs K.-U. and Elvert M. (2014) Carbon isotope equilibration during sulphate-limited anaerobic oxidation of methane. *Nature Geoscience* **7**, 190–194.

Young E. D. (2019) A Two-Dimensional Perspective on CH4 Isotope Clumping: Distinguishing Process from Source. In *Deep Carbon* (eds. B. N. Orcutt, I. Daniel, and R. Dasgupta). Cambridge University Press. pp. 388–414.

Young E. D., Kohl I. E., Lollar B. S., Etiope G., Rumble D., Li (李姝宁) S., Haghnegahdar M. A., Schauble E. A., McCain K. A., Foustoukos D. I., Sutclife C., Warr O., Ballentine C. J., Onstott T. C., Hosgormez H., Neubeck A., Marques J. M., Pérez-Rodríguez I., Rowe

A. R., LaRowe D. E., Magnabosco C., Yeung L. Y., Ash J. L. and Bryndzia L. T. (2017) The relative abundances of resolved l2 CH 2 D 2 and 13 CH 3 D and mechanisms controlling isotopic bond ordering in abiotic and biotic methane gases. *Geochimica et Cosmochimica Acta* **203**, 235–264.

Declaration of interests

☒ The authors declare that they have no known competing financial interests or personal relationships that could have appeared to influence the work reported in this paper.

☐The authors declare the following financial interests/personal relationships which may be considered as potential competing interests: